

Large eddy simulation of three-dimensional vortex structures in cnoidal waves over a submerged step

Aristos Christou, Thorsten Stoesser & Zhihua Xie

To cite this article: Aristos Christou, Thorsten Stoesser & Zhihua Xie (2025) Large eddy simulation of three-dimensional vortex structures in cnoidal waves over a submerged step, Journal of Hydraulic Research, 63:3, 297-319, DOI: [10.1080/00221686.2025.2476432](https://doi.org/10.1080/00221686.2025.2476432)

To link to this article: <https://doi.org/10.1080/00221686.2025.2476432>



© 2025 The Author(s). Published by Informa UK Limited, trading as Taylor & Francis Group.



Published online: 08 May 2025.



Submit your article to this journal [↗](#)



Article views: 140



View related articles [↗](#)



View Crossmark data [↗](#)

Large eddy simulation of three-dimensional vortex structures in cnoidal waves over a submerged step

Aristos Christou ^a, Thorsten Stoesser ^b and Zhihua Xie ^a

^aSchool of Engineering, Cardiff University, Cardiff, UK; ^bDepartment of Civil, Environmental and Geomatic Engineering, University College London, London, UK

ABSTRACT

A three-dimensional (3D) numerical wave tank based on large eddy simulations (LES) is employed to study the interaction of a submerged rectangular step with periodic waves in shallow water depths, with a good agreement with experimental measurements. The effect of step height is studied in terms of wave elevations, vorticity field and 3D vortical structures. The shallow and intermediate cases have limited effect on the water surface fluctuations both upstream and downstream from the structure whereas a dominant wave–structure interaction is observed in the steep case, resulting in wave breaking downstream from the step. The effect of step height variation on 3D vortical structures is also investigated in detail and results suggest that three dimensionality is almost negligible in the shallower step whereas in the remaining cases, dominant 3D effects are formed generating discontinuities in the primary spanwise eddies and forming small billows with zero spanwise vorticity interacting with the floor bed, the structure and the water surface.

ARTICLE HISTORY

Received 9 September 2024
Accepted 28 February 2025

KEYWORDS

cnoidal waves; large eddy simulations; numerical wave tank; submerged step; wave–structure interaction; vortex generation

1. Introduction

Breakwaters are installed and operated at shallow water depths close to the coastline with high human and ecological activity. In submerged breakwaters, waves are effectively dissipated, protecting the coastline from extreme wave conditions, minimizing negative ecological impact and reducing visual pollution.

The increasing recurrence of extreme wave conditions due to global warming, the effort towards sustainability together with the negative impact of large inland power plants have led to the increasing demand for further offshore energy exploitation and more cost-effective and durable offshore and coastal structures. Researchers have conducted numerical and experimental studies to study the interaction of realistic sea conditions with offshore structures in an attempt to analyse and understand the local hydrodynamics involved and how these affect the functionality and durability of the structure under test. Martins et al. (2009) provided an extensive report on the effect of near-coast structures and breakwaters on the local environment, suggesting that anthropogenic activities can have important ecological as well as energetic consequences for the functioning of the local ecosystem. Kramer et al. (2005) conducted small and large scale experiments with waves propagating over low-crested structures, and measured wave elevations as well as the local velocity fields used to study the structures' efficiency and its impact on the surrounding ecological environment. Similarly, Chang

et al. (2001) carried out experiments on a solitary wave propagating over a submerged step where the local velocity and vorticity field were recorded, and extended their study later in Chang et al. (2005) where the step was set under the action of periodic cnoidal waves. Christou et al. (2008) conducted experiments on periodic nonlinear waves propagating over a step at various wave steepness to investigate the effect of step's size and geometry on reflected waves. In the same study simulations based on the boundary element method (BEM) were conducted and results were compared with the experimental measurements. Ting et al. (2016) ran a series of experiments of different wave conditions propagating over a step with various heights and widths. Water surface variations in time and space were recorded and conclusions on the effect of various geometrical parameters were made. For example, they found that the ratio of submergence depth to water depth is most important in generating higher harmonic fluctuations while the width of the step has almost zero effect. Brocchini et al. (2022) carried out particle tracking velocimetry (PTV) measurements to study the interaction between counter-rotating vortices generated by wave breaking and bed discontinuity.

Numerical methods have also been employed to investigate similar problems. Ning et al. (2008) used a higher order boundary element model (HOBEM) to generate realistic wave conditions inside a tank whereas Liu et al. (2009) utilized the desingularized boundary

integral equation Method (DBIEM) both based on the potential flow theory to simulate the progression of waves inside a tank. Additionally, Agarwal et al. (2022) and Liu and Wang (2020) employed a numerical wave tank based on the particle method to simulate wave–structure interaction, while a Lagrangian-based numerical model (Buldakov et al., 2019; Chen et al., 2019) was employed to simulate the generation of extreme wave groups and the interaction of waves with piercing structures and depth-varying currents.

Improvement in computational resources favoured the utilization of the Navier–Stokes (NS) equations to develop computational fluid dynamics (CFD) based numerical wave tanks to investigate wave–structure interactions and perform a detailed analysis of the turbulent flow structure evolution and local hydrodynamic characteristics. The volume-average Reynolds-averaged Navier–Stokes (RANS) method was employed by Lara et al. (2008), in which experimental measurements were used to validate the model followed by simulations to examine the interaction of waves with low-mound breakwaters. Similarly, a large eddy simulation (LES) based numerical wave tank (NWT) was developed in Xie et al. (2020) based on the volume-of-fluid (VOF) method and the Cartesian cut-cell method to represent solid structures inside a numerical tank interacting with various wave conditions. Additionally Hur et al. (2012) performed investigations of submerged dual breakwaters interacting with incoming waves, utilizing the LES method. Similarly, the LES method coupled with the VOF method was also employed in Chu et al. (2022) to calculate the forces acting on submerged decks, while validations were performed based on experiments conducted in the same study. In addition to the experiments in Chang et al. (2005), simulations were conducted using the open-source OpenFOAM software to investigate the formation of rotational flow structure near a submerged step using the RANS method.

In the past, some researchers have conducted numerical simulations to investigate the interaction of waves with submerged rectangular obstacles. Tripepi et al. (2020) conducted experiments and simulations of a solitary wave propagating over a square barrier. A smoothed-particle hydrodynamics (SPH) model was employed to calculate the water surface evolution and the forces acting on the structure and results were validated against experimental data. Additionally, the local flow was studied in terms of vortex shedding near the rectangular step during the progression of the solitary wave. Lin and Huang (2010) employed a numerical model based on the Lagrangian method to investigate the vortex shedding of a solitary wave propagating over a submerged step on a two-dimensional framework and studied the effect of wave height on eddy formation. Similarly, Lin (2004) studied the interaction of a two-dimensional solitary wave with a submerged

step using the energy integral equation to investigate the wave reflection transmission and dissipation of the water surface based on several wave heights. The oscillating flow imposed by periodic waves generates local complex flow characteristics not being observed in solitary wave flows. For example, Hsu et al. (2004) employed the RANS method to simulate the progression of waves over double-submerged breakwaters. In the same study, the generation and dissipation of vortical structures near the submerged steps were under investigation in a two-dimensional numerical domain. Additionally, a two-dimensional Helmholtz decomposition method was employed in Lin and Huang (2009) to simulate the interaction of waves with submerged structures. In the same study, the authors investigated the local flow field in terms of velocity vector field and contours of the vortex shedding near the edges of a submerged rectangular step. Chang et al. (2005) conducted experiments and simulations of cnoidal waves propagating over a rectangular submerged step. In their study, the authors employed a two-dimensional numerical wave tank based on the RANS method and studied the local velocity field and vortex formation. Overall, studies published in the past examined the effect of linear and nonlinear waves past submerged structures based on various numerical techniques. However, most of the studies did not take into account the three-dimensionality of the problem. The majority of the studies adopted simplified numerical models and did not report on the detailed flow field evolution near the structure.

The objective of this study is to use LES to study the local vorticity field, free surface dynamics and three-dimensionality effects near a submerged step of various heights under the action of cnoidal waves in shallow water depths. These have rarely been investigated in the literature and are different from single deep-water breaking waves in a periodic domain (Mostert et al., 2022). The above objectives are to be resolved based on the LES method in an attempt to improve our understanding of the effect of turbulent flow structures in such wave–structure interaction applications in various aspects such as in wave damping, wave breaking, three-dimensional effects and seabed sediment transport which will lead to improved offshore structures such as wave breakers and wave energy converters. In the remaining text, the numerical background of the current NWT is briefly described in Section 2. In Section 3 the simulations conducted to investigate the current problem are described including validations based on a previous experimental study followed by discussions of results of water surface fluctuations, local vorticity field and three-dimensional representation of rotational flow structures. Lastly, Section 4 summarizes the conclusions based on the current simulations and emphasizes the effect of step height in such applications.

2. Large eddy simulations

2.1. Flow solver

The three-dimensional numerical wave tank, referred to as Hydro3D-NWT (Christou, Stoesser, et al., 2021), is employed to simulate the interaction of cnoidal waves with a submerged step. The accuracy of the code has been examined in previously published studies for various offshore and coastal applications such as regular waves over bars and solitary waves over thin flat plates (Christou et al., 2020; Christou, Xie, et al., 2021). The current code solves the spatial filtered incompressible Navier–Stokes equations using the method of large eddy simulations (Cevheri et al., 2016; Fraga et al., 2016; Stoesser et al., 2015) on a uniform Cartesian grid as:

$$\frac{\partial \bar{u}_i}{\partial x_i} = 0 \quad (1)$$

$$\begin{aligned} \frac{\partial \bar{u}_i}{\partial t} + \frac{\partial \bar{u}_i \bar{u}_j}{\partial x_j} = & -\frac{1}{\rho} \frac{\partial \bar{p}}{\partial x_i} + \frac{\partial}{\partial x_j} \left(\nu \frac{\partial \bar{u}_i}{\partial x_j} \right) \\ & - \frac{\partial \tau_{ij}^{SGS}}{\partial x_j} + f_i + g_i + F_i^{sf} \end{aligned} \quad (2)$$

where the bar ($\bar{\cdot}$) represents spatial filtered variables. \bar{u}_i is the velocity field in x_i direction, \bar{p} the pressure field and ρ and ν are the fluid density and kinematic viscosity, respectively. g_i is the external force due to gravity, F_i^{sf} is the surface tension force and f_i is the force imposed on fluid cells to enforce a no-slip boundary condition on solid structures. This is achieved using the immersed boundary (IB) method from Uhlmann (2005). The spatial derivatives in Equations (1) and (2) are solved using finite difference schemes. For example, 4th-order central differences are used for the convective terms whereas 2nd-order central differences are employed for the diffusive terms. The Navier–Stokes equations are solved using the fractional step method as in Chorin (1968) coupled with a 3rd-order Runge–Kutta scheme. In LES, small flow structures greater than the cutoff wavelength k_{cutoff} are modelled using an eddy viscosity ν_t model and as a result the term τ_{ij}^{SGS} , also referred to as the sub-grid scale (SGS) tensor, appears in the above equations. The dissipative effect of such small scale flow structures is modelled in this study using the wall adapting local eddy (WALE) model presented in Nicoud and Ducros (1999) and employed as follows:

$$\nu_t = (C_w \Delta)^2 \frac{(S_{ij}^d S_{ij}^d)^{3/2}}{(\bar{S}_{ij} \bar{S}_{ij})^{5/2} + (S_{ij}^d S_{ij}^d)^{5/4}} \quad (3)$$

where C_w is a constant set to $C_w = 0.46$ and Δ the filter size which in this study is set to $\Delta = (dx \, dy \, dz)^{1/3}$. The eddy viscosity is calculated using the resolved velocity field tensor $\bar{g}_{ij} = \frac{\partial \bar{u}_i}{\partial x_j}$ as:

$$\bar{S}_{ij} = \frac{1}{2} \left(\frac{\partial \bar{u}_i}{\partial x_j} + \frac{\partial \bar{u}_j}{\partial x_i} \right) \quad (4)$$

and

$$S_{ij}^d = \frac{1}{2} (\bar{g}_{ij}^2 + \bar{g}_{ji}^2) - \frac{1}{3} \delta_{ij} \bar{g}_{kk}^2 \quad (5)$$

where $\bar{g}_{ij}^2 = \bar{g}_{ik} \bar{g}_{kj}$. Finally, the total fluid viscosity is updated utilizing the eddy viscosity and fluid viscosity as $\nu_T = \nu + \nu_t$.

2.2. Free-surface

To simulate multi-phase applications the level-set method (LSM) proposed by Osher and Sethian (1988) is adopted to capture the interface between the two phases. In this method, a signed distance function ϕ is defined throughout the domain as:

$$\phi(x, t) \begin{cases} < 0, & \text{if } x \in \Omega_{gas} \\ = 0, & \text{if } x \in \Gamma \\ > 0, & \text{if } x \in \Omega_{liquid} \end{cases} \quad (6)$$

where negative ϕ values denote grid cells in air, positive values are grid cells in water and cells with zero ϕ values draw the interface of the two. Originally, ϕ is the distance measured from the fluid cell's centre to the water surface and is initialized to still water conditions. A Heaviside function $H(\phi)$ is defined based on Equation (7) near the water surface inside a layer of 2ε , where $\varepsilon = 2 \max(dx, dy, dz)$ to avoid discontinuities from sharp gradients of the fluid density and viscosity, which are then updated as:

$$H(\phi) \begin{cases} = 0, & \text{if } \phi < -\varepsilon \\ = \frac{1}{2} \left(1 + \frac{\phi}{\varepsilon} + \frac{1}{\pi} \sin \frac{\pi \phi}{\varepsilon} \right), & \text{if } |\phi| \leq \varepsilon \\ = 1, & \text{if } \phi > \varepsilon \end{cases} \quad (7)$$

$$\rho(\phi) = \rho_g + (\rho_l - \rho_g)H(\phi)$$

$$\nu(\phi) = \nu_g + (\nu_l - \nu_g)H(\phi) \quad (8)$$

The new location of the water surface is calculated based on the velocity field at previous time steps by solving the following advection equation using a 5th-order weighted essentially non-oscillatory (WENO) scheme for spatial derivatives followed by a re-initialization technique as in Sussman et al. (1994):

$$\frac{\partial \phi}{\partial t} + u_i \frac{\partial \phi}{\partial x_i} = 0 \quad (9)$$

2.3. Numerical wave tank

In this study, waves are generated in the west boundary (inlet) using Dirichlet boundary conditions based on the kinematics obtained from analytical solutions of various wave theories. The current NWT can generate nonlinear waves of up to 5th-order Stoke wave theory, focused waves, cnoidal and solitary waves. For the generation of cnoidal waves, wave elevations and the wave-induced velocities from Wiegel (1960) are

imposed at the inlet boundary. For example, the water surface is initialized and set every time step according to the following:

$$\phi \begin{cases} = |z_c - \eta|, & \text{if } z_c < \eta \\ = -|z_c - \eta|, & \text{if } z_c > \eta \\ = 0, & \text{if } z_c = \eta \end{cases} \quad (10)$$

where z_c is the vertical coordinate at the centre of the grid cell and n is the water surface elevation with $n = 0$ at still water level.

Waves are absorbed in the east boundary using the relaxation method proposed by Mayer et al. (1998), also referred to as numerical beach, similar to physical wave flumes. Absorbing incident waves is crucial in such applications since potential reflected waves interacting with incident waves will alter the wave conditions and affect the results for the overall case. Based on the method employed here, the water surface and velocity field are gradually set to still water conditions over a relaxation zone, usually two wavelengths long, implemented as:

$$\Gamma(X) = 1 - \frac{e^{X^R} - 1}{e - 1}, \quad X = \frac{x - x_s}{x_e - x_s} = [0, 1] \quad (11)$$

where $\Gamma(X)$ is the damping function, R a constant set to $R = 3.5$ where x_s and x_e are the horizontal coordinates of the relaxation zone's starting and ending points, respectively. The water surface, in terms of the signed distance function ϕ , and the velocity components are gradually set to the targeted value (in this case $\phi_{target} = 0$ at $z = d$ and $u_i = 0.0$) as:

$$\phi = (1 - \Gamma(X))\phi_{target} + \Gamma(X)\phi_{computed} \quad (12)$$

$$u_i = (1 - \Gamma(X))u_{i,target} + \Gamma(X)u_{i,computed} \quad (13)$$

The above method has been examined in a previous study by Christou, Stoesser, et al. (2021) where steep waves were generated inside a numerical tank for a long period and the wave elevation in space and time was plotted and compared with analytical solutions.

2.4. Surface tension

Continuum surface force (CSF) model

To study wave–structure interaction problems, a surface tension model is employed to accurately simulate wave breaking, air entrainment and the formation of small bubbles and droplets. For this reason, a continuum surface force model described in Sussman et al. (1994) has been implemented in Hydro3D-NWT. In CSF models the surface tension force F_i^{sf} is defined as follows:

$$F_i^{sf} = \sigma k \delta(\phi) n_i \quad (14)$$

where σ is the surface tension coefficient, k the curvature of the water surface and $\delta(\phi)$ a modified delta

function similar to Equation (7) to smooth the surface force across the transition zone throughout the water surface. Here k , n_i and $\delta(\phi)$ are calculated using the signed distance function ϕ from LSM, according to the following equations:

$$k = -\nabla n_i, \quad n_i = \frac{\nabla \phi}{|\phi|} \quad (15)$$

and

$$\delta(\phi) \begin{cases} = \frac{1}{2} \left(1 + \cos \frac{\pi \phi}{\varepsilon} \right), & \text{if } |\phi| < \varepsilon \\ = 0, & \text{if else} \end{cases} \quad (16)$$

ε is the extension of the transition zone at each phase and has the same length as in Equation (7). A modified method for calculating the surface tension is adopted in the current code based on a density-scaled, delta function $\delta^{scaling}$ (Yokoi et al., 2016). This method shifts the delta function towards the higher-density fluid and improves the stability of the model.

$$F_i^{sf} = \sigma k \delta^{scaling}(\phi) n_i, \quad \delta^{scaling} = 2H(\phi)\delta(\phi) \quad (17)$$

The derivatives of ϕ in Equation (15) are calculated based on 2nd-order central differences at the centre of the cell where k , n_i and $\delta(\phi)$ are also defined. Simple interpolation is then used to calculate these values at the faces of the cell.

3. Cnoidal waves over a submerged step

In this section, the results obtained from simulations of cnoidal waves propagating over a rectangular step in shallow water depth are reported. First, the experimental study conducted by Chang et al. (2005) is simulated to examine the capability of the code in reproducing accurate wave–structure interactions in shallow water depths. Then in the following sections, a detailed representation of the effect of various step heights on local hydrodynamics such as instant vorticity and vorticity magnitude as well as three-dimensional turbulent flow structures is discussed.

3.1. Computational setup

Figure 1 shows a 25.6 m long, 0.48 m deep and 0.6 m wide numerical wave tank utilized to simulate cnoidal waves of wave height $H/d = 0.15$, wave period $T = 2.0$ s and wavelength $L/d = 12.375$, where $d = 0.24$ m is the still water level, propagate over a rectangular step. The submerged step is fixed at $x = 12.6$ m from the wave maker with a total length of $A = 0.4$ m extending throughout the total width of the domain. In the experiments two step heights (D) were considered, $D/d = 0.25$ and $D/d = 0.5$; however, here an additional step height of $D/d = 0.75$ is considered to investigate the effect of a structure located very close to

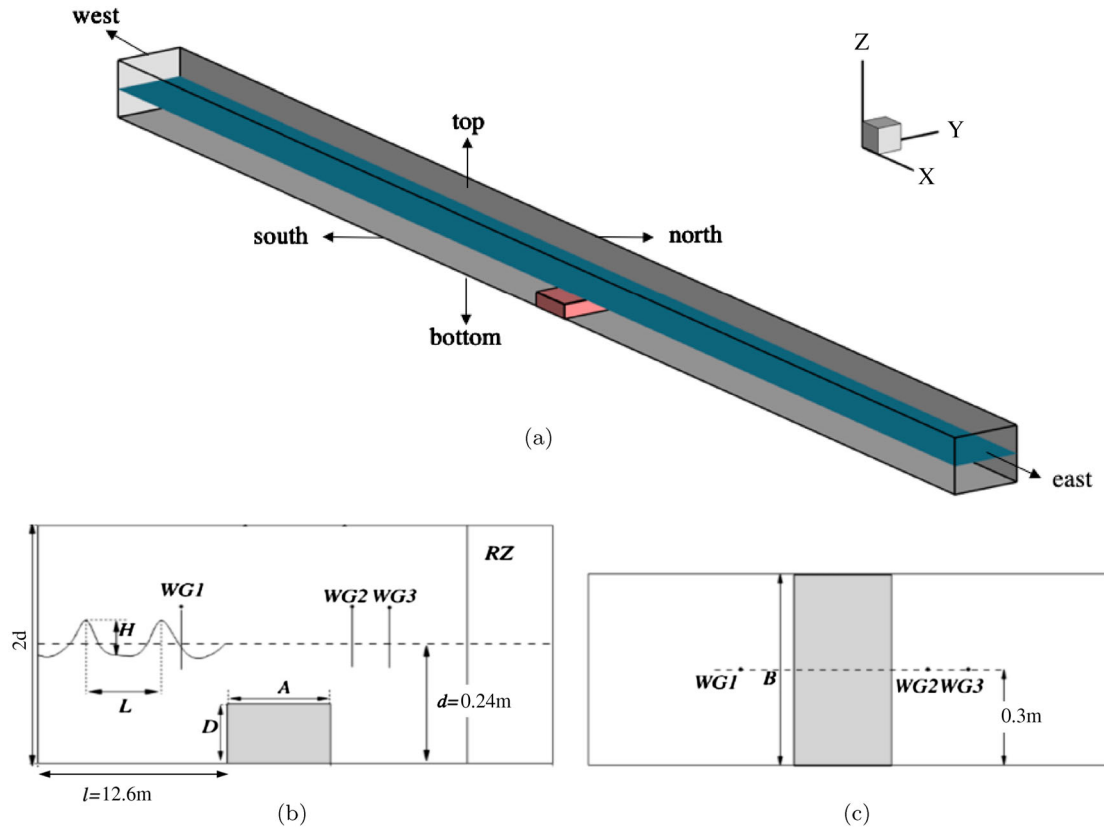


Figure 1. A schematic diagram of the numerical domain. (a) 3D representation (b) side view and (c) top view.

Table 1. Boundary conditions.

	West	East	Top	Bottom	South/north
\bar{u}_i	Dirichlet	Relaxation zone/Neumann	Free-slip	No-slip	Free-slip
\bar{p}	Neumann	Neumann	Neumann	Neumann	Neumann
ϕ	Dirichlet	Relaxation zone/Neumann	Neumann	Neumann	Neumann

the water surface. Three wave gauges are aligned over the centreline of the tank to record the water surface fluctuations upstream and downstream from the submerged step at $x = 4.8$ m (WG1), $x = 13.15$ m (WG2) and $x = 14.5$ m (WG3).

Table 1 lists the boundary conditions employed to simulate the current problem in which west and east boundaries serve as a wave maker and numerical beach, respectively, while a Neumann condition is set for the filtered pressure field in all boundaries. The following simulations are conducted using a fine uniform grid of $dx = dy = 0.003$ m and $dz = 0.0015$ m (or $dx/d = dy/d = 0.0125$ and $dz/d = 0.00625$) resulting in $N_{tot} = 400 \times 10^6$ grid cells and fixed time step of $dt = 0.0005$ s to ensure that the Courant–Friedrichs–Lewy (CFL) number is always less than 0.2 ($CFL \leq 0.2$). Waves are generated for around 22 s and the first four waves are ignored from the following figures to ensure that the waves and the near-structure flow field are fully developed. The domain is divided into 128 sub-domains and memory is shared between blocks by Message Passing Interface (MPI). For each case of the following section, 128 CPUs are used and the computational time needed to simulate

10 s of wave propagation is 24 hours. The spatial and temporal resolution adopted here has been chosen after conducting various convergence studies of the same problem of a single case ($D/d = 0.5$) and the present code was applied in thorough validation applications in Christou, Stoesser, et al. (2021).

3.2. Validation

First, waves are generated in the absence of the structure to ensure Hydro3D-NWT can reproduce accurate wave conditions inside the tank similar to the experiments. The wave elevations plotted here are normalized with the wave height as n/H where $n = 0$ at $z = d$. Figure 2 plots the time history of the wave elevations recorded over the step's leading edge together with the analytical solution employed for boundary conditions (theoretical) and experimental measurements and a good agreement between the cases is achieved.

The step is then introduced inside the tank and wave elevations at the three WG locations are recorded. Figure 3 shows the simulated wave elevations (solid lines) and the experimental measurements (open circles) as recorded over the last five wave periods

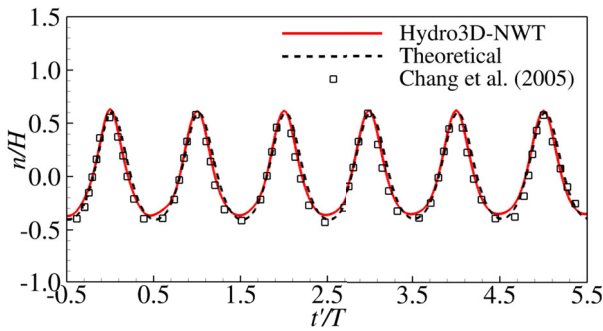


Figure 2. Comparisons of simulated wave elevations (solid red lines) with analytical solutions (Wiegel, 1960, dashed lines) and experiments (Chang et al., 2005, open squares) at the step's leading edge location in the absence of the structure, at $x = 12.6$ m.

considering the case with a step height of $D/d = 0.5$. Results from a RANS model published in the same study as the experiments (Chang et al., 2005) are plotted together with the current LES model to compare the two approaches in capturing the wave–structure interactions. Normalized wave elevations agree well with the experimental measurements in all locations. In Figure 3a the undisturbed wave train upstream from the structure is in good agreement with the experiments while no dispersion errors are observed. Figure 3b plots the water surface fluctuations just downstream from the

submerged step's trailing edge where simulations and experiments are in very good agreement. At this location, the crest level increases and becomes narrower and forms a backwards slope towards the wavemaker due to the immediate change of the water depth as the wave propagates over the step. Further downstream, at $x = 14.5$ m (Figure 3c), the wave crest level is slightly reduced and secondary peaks on the wave troughs are formed due to higher harmonic waves being reflected from the step. Overall wave elevations agree well with experiments in all locations inside the tank when a step height of $D/d = 0.5$ is considered. Additionally, results obtained from the LES based simulations are also in good agreement with the RANS model. Slight variations are observed at the location of WG1 (Figure 3a) where the wave trough is at a lower level for RANS model. This may be due to different approaches used for turbulence modelling and also in generating waves inside the tank.

Additionally, the capability of the code to accurately capture the formation of vortical flow structures is examined in terms of the maximum positive and negative absolute values of y -component vorticity (inside the page). Here, positive vorticity is defined by counterclockwise rotation. Figure 4 plots the maximum magnitude of the positive (red) and negative (blue) vorticity recorded at the leading edge (upper)

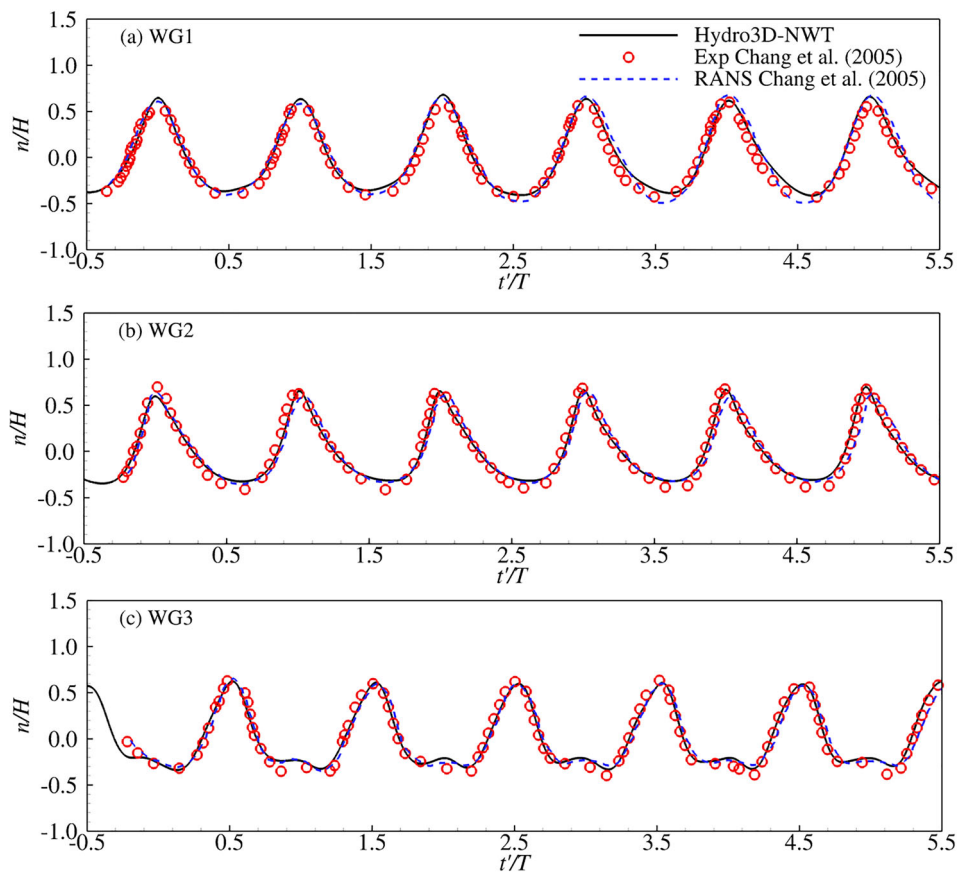


Figure 3. Comparisons of the simulated LES wave elevations (solid black lines), RANS (dashed blue lines) and experiments (open circles) at (a) WG1, (b) WG2 and (c) WG3. $D/d = 0.5$.

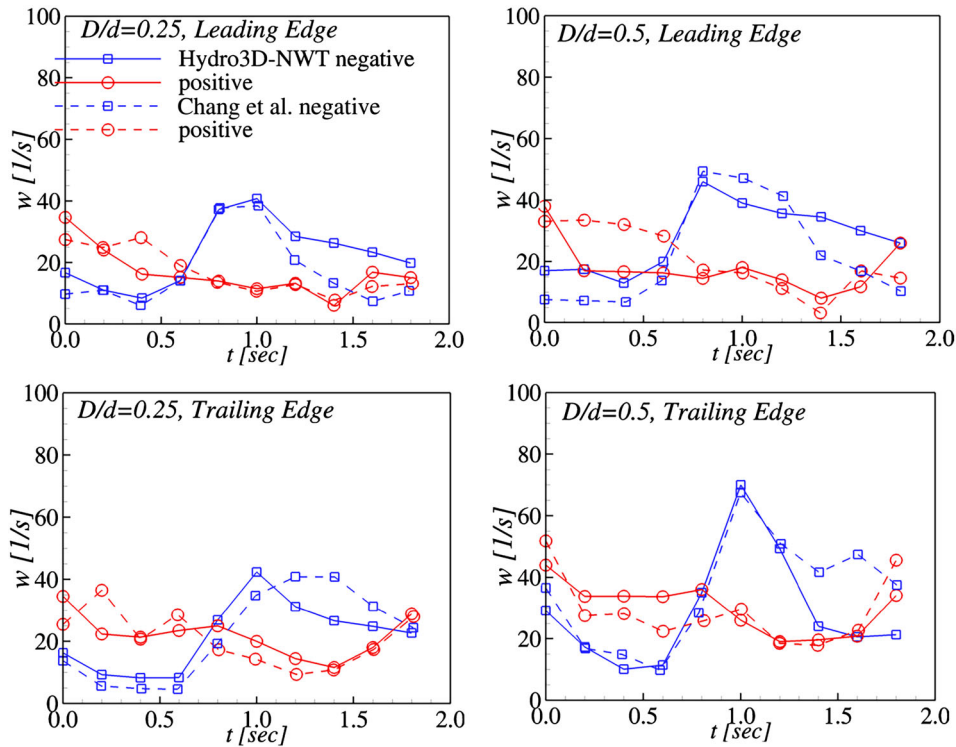


Figure 4. Maximum vorticity magnitude of the $D/d = 0.25$ (left) and $D/d = 0.5$ (right) of the positive (red) and negative (blue) eddies near the step's leading edge (top panel) and trailing edge (lower panel). Positive vorticity is considered counterclockwise rotation. LES results are compared with experimental measurements from Chang et al. (2005).

and trailing edge (lower) for the $D/d = 0.25$ case (left panel) and $D/d = 0.5$ case (right panel). The vorticity values plotted in this figure are calculated based on phase averaging over five wave periods to account for discrepancies between wave components. Simulations (solid lines, open squares) are plotted together with the corresponding experiments (dashed lines, open circles) over one wave period. Considering first the leading edge (Figure 4 top panel), the trend of the magnitude of the counterclockwise (positive) vorticity is well captured by Hydro3D-NWT, where better results are observed in the case of $D/d = 0.25$, whereas the positive eddy is slightly underestimated in the $D/d = 0.5$ case at $0.2 \leq t \leq 0.6$ after which simulations and experiments (Chang et al., 2005) are in good agreement. The magnitude as well as the evolution of the negative vorticity over the leading edge is well captured by the current NWT for both step heights. Over the leading edge, positive and negative vortices have smooth transitions between minimum and maximum values and when the counterclockwise eddy's vorticity magnitude is maximum, the clockwise eddy is dissipated until is formed again from the following wave.

Similarly, the simulated vorticity magnitude near the trailing edge (Figure 4 lower panel) matches well with the experimental measurements throughout the wave propagation in both step heights. Better results are achieved in the progression of the positive eddy; however, the peak of the negative vorticity is captured well in both step heights. The intensity of the clockwise

vortex in the case of $D/d = 0.5$ is underestimated at the end of the wave propagation, which might be partly due to different waves used between the experiments and the simulations. This argument is further supported by the simulated vorticity at the beginning of the wave which agrees very well with the experiments. In general, results show that Hydro3D-NWT can accurately capture the fluctuation of the water surface and the evolution of the vortex shedding in the leading and trailing edge of the step at various step heights. In the latter, simulations slightly vary from the experiments in specific time instances due to different interactions between various wave components and inconsistency in the measurement of vorticity magnitude between simulations and experiments.

3.3. Wave elevations

This section examines the effect of the step's height on the water surface fluctuations and its impact on the wave-structure interaction. Figure 5 shows the time history of the wave elevations recorded at the three wave gauge locations (left panel) together with the amplitude energy spectrum of the water surface fluctuations (right panel) and comparisons are made between $D/d = 0.25$ (red lines), $D/d = 0.5$ (black lines) and $D/d = 0.75$ (blue lines). Figure 5a plots the water surface fluctuations upstream from the structure at which the submerged structure has no significant effect on wave elevations. After $t'/T \geq 1.5$ the effect of the submergence

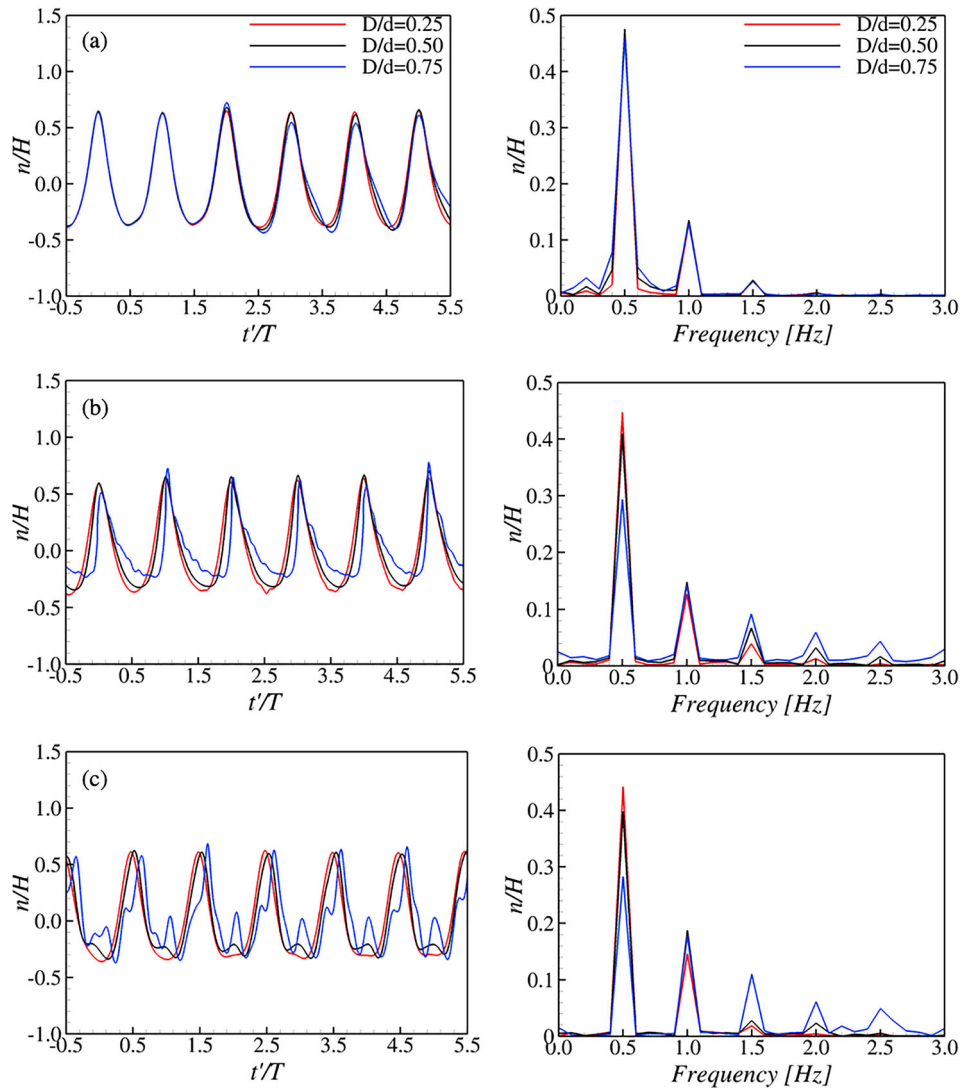


Figure 5. Time history of the wave fluctuations (left panel) and the corresponding amplitude energy spectrum (right panel) as recorded at (a) WG1, (b) WG2 and (c) WG3 for $D/d = 0.25$ (red lines), $D/d = 0.5$ (black lines) and $D/d = 0.75$ (blue lines).

structure starts to appear with variations in the crest level and trough shape. These are mainly observed in the case of $D/d = 0.75$ in which small reflected waves are formed propagating in the opposite direction and slightly alter the wave period and wave elevations. Additionally, no distinct variations are observed in the energy spectrum calculated in the same location. A primary amplitude is observed at $f = 0.5$ Hz corresponding to the wave period ($T = 2.0$ s) with higher harmonics formed at $f = 1.0$ Hz and $f = 1.5$ Hz.

In Figure 5b the wave elevations are recorded just downstream from the step's trailing edge. At this location, the effect of the step's height is significant on the water surface fluctuations with the main variations observed in the steepest case ($D/d = 0.75$). In the other two cases ($D/d = 0.25$ and $D/d = 0.5$) the waves propagating over the step remain mostly unchanged and are not affected by the presence of the submergence step. In contrast to the shallower step cases, when the $D/d = 0.75$ case is considered the initial wave shape is altered due to the immediate change in

the effective water depth. As a result, the crest level slightly increases whereas the trough level decreases and the waves become narrower towards the crest. These changes are also observed in the energy amplitude spectrum at which the primary peak is reduced by 35% at $f = 0.5$ Hz and the remaining higher harmonics are slightly increased especially after $f \geq 1.5$ Hz. A similar trend is observed in the $D/d = 0.5$ case but to a much lower degree.

At the WG3 location (Figure 5c) the submerged step has a maximum effect on the water surface fluctuations apart from the shallower case ($D/d = 0.25$) in which waves remain almost unchanged throughout the tank. Considering the intermediate step height case ($D/d = 0.5$), the crest level is slightly decreased and a secondary peak is formed on the trough level of the wave. This is also observed in the amplitude spectrum where the primary amplitude at $f = 0.5$ Hz is decreased and the higher harmonics slightly increase. In the $D/d = 0.75$ case wave elevations suggest that wave breaking occurs at some point downstream from the trailing

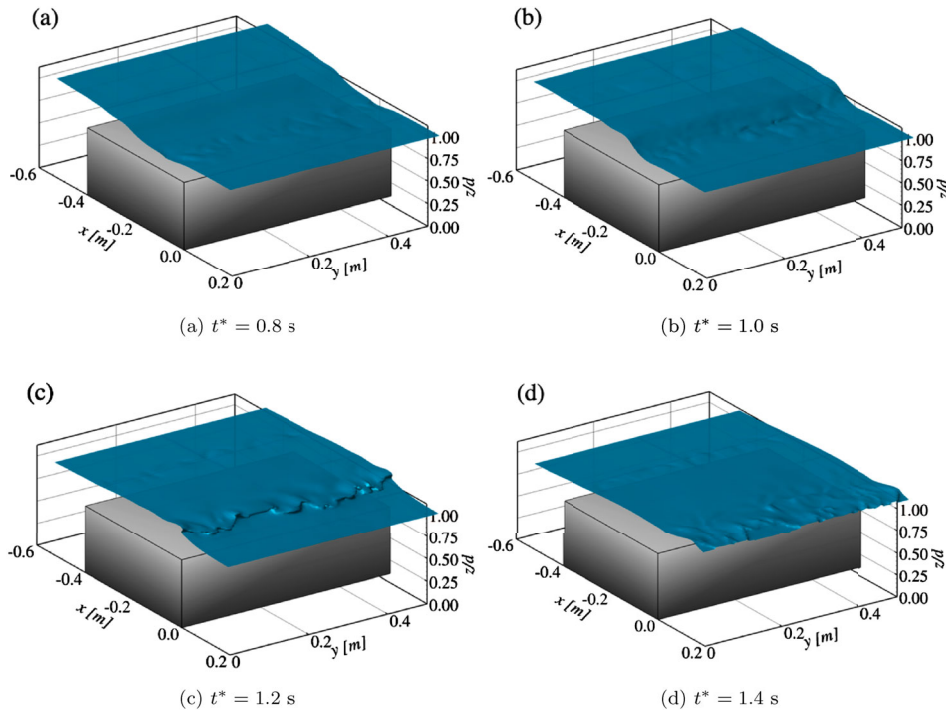


Figure 6. Screenshots of the water surface in terms of the iso-surface at $\phi = 0$ for $D/d = 0.75$. (a) $t^* = 0.8$ s. (b) $t^* = 1.0$ s. (c) $t^* = 1.2$ s and (d) $t^* = 1.4$ s.

edge and higher harmonic water surface fluctuations are observed due to smaller waves formed after wave breaking. The crest level shifts forward and relatively large peaks are formed in the trough level. The wave elevation trend slightly varies between wave components due to the random and nonlinear interactions that occur during wave breaking. It is worth noting that in the corresponding amplitude spectrum plot, the first harmonic is further decreased, partly due to energy dissipation during wave breaking and higher harmonic increases due to the formation of smaller waves.

3.4. Water surface dynamics

To further investigate the present wave–structure interaction, the progression of the water surface in space for a step height of $D/d = 0.75$ is examined since previous results suggest that it has maximum effects and that wave breaking occurs. In the following figures coordinate x is set to zero at the step's trailing edge and z is normalized with water depth d . Figure 6 demonstrates the evolution of the near structure water surface in terms of the iso-surfaces at $\phi = 0$ at various time steps over one wave period. Here a new time variable t^* is defined as $t^* = t - 22.05$ s which is the time at which the last wave recorded in these simulations passes over the step's leading edge. It is clear from this figure that when a step height of $D/d = 0.75$ is considered under these wave conditions wave breaking occurs at 0.2 m downstream from the step's trailing edge at about $t^* = 1.2$ s. When the wave reaches the step's leading edge (Figure 6a) the wave height increases

due to the decreased water depth which then slightly decreases over the trailing edge. The latter is a result of the accelerated negative flow as the wave builds up over the submerged structure. While the wave propagates just over the step (Figure 6b), the wave height increases and starts to form a forward tip before it breaks moments later at $t^* = 1.2$ s (Figure 6c). The three-dimensional water surface fluctuations presented in this figure are a result of the increased velocities at the wave's forward jet and the nonlinear physics involved in wave breaking. At $t^* = 1.4$ s (Figure 6d) the water surface remains disturbed after wave breaking occurs partly due to smaller wave formation and reflection and partly due to the interaction of submerged rotational flow structures formed at the step's trailing edge (more discussion on this in the next sections).

3.5. Vorticity field

In the following figures, the near-structure flow field and the effect of the step's height are examined in terms of y vorticity (ω_Y). Here we only present the vorticity field as calculated on each fluid cell at the centre of the flume at $y = B/2 = 0.3$ m in a x - z plane to visualize the actual vorticity field and will demonstrate the three-dimensionality of the turbulent flow in the following figures. Figure 7 demonstrates the areas at which the flow evolution and vorticity field are visualized near the leading and trailing edge, leading edge volume (LEV) and trailing edge volume (TEV), respectively measuring 12×12 cm² with the edge in each case located at the centre of the frame.

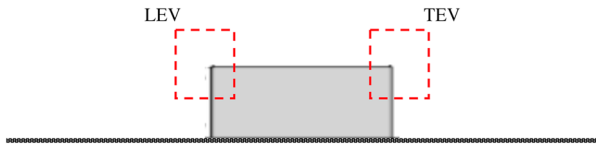


Figure 7. Representation of the leading edge volume (LEV) and trailing edge volume (TEV) zones of interest.

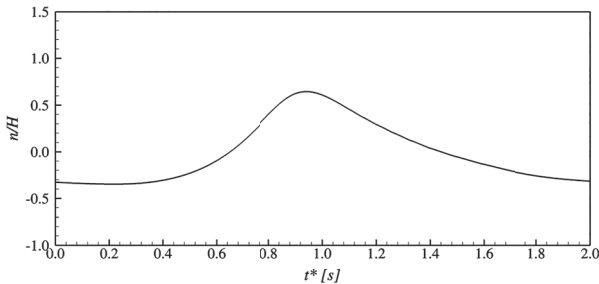


Figure 8. Wave elevation over the leading edge ($x = 12.6$ m) where $t^* = 0.0$ s is set at when $t = 22.05$ s.

Leading edge

Figure 8 plots the exact location of the water surface over the leading edge (at $x = 12.6$ m) to support the discussion of the vortex shedding and eddy formation. Figure 9 shows the vorticity field near the leading edge for the three step cases considered here, $D/d = 0.25$ (left panel), $D/d = 0.5$ (middle panel) and $D/d = 0.75$ (right panel) plotted over one wave period with a time interval of $\Delta t = 0.2$ s. The vorticity field is plotted in terms of vorticity contour lines with solid lines demonstrating counterclockwise vorticity (positive) and dashed lines clockwise vorticity (negative). Here, $t^* = 0.0$ s is related to $t = 22.05$ s at which the last wave approaches the step's leading edge. Additionally Figure 10 plots the maximum magnitude of the vorticity near the leading edge for the same time steps. In general, the formation of eddies at the leading edge is similar between the shallower cases ($D/d = 0.25$ and $D/d = 0.5$), whereas variations are observed in the $D/d = 0.75$ case as a result of the increased velocities under the water surface. In the case of cnoidal waves, particle velocities increase with decreasing water depth and as a result the formation of new eddies varies between different step heights. For instance, the horizontal and vertical velocity components are higher at the $D/d = 0.75$ step's leading edge compared to the other cases and hence the formation of more energetic eddies is observed.

In Figure 9a the negative flow (from right to left) imposed by the wave trough over the leading edge generates a positive eddy on the left side of the step that drifts further upstream from the structure at $t^* = 0.2$ s (Figure 9b). At $t^* = 0.4$ s (Figure 9c) the wave crest approaches the step, generating a positive flow (from left to right) and as a result, the positive eddy formed at previous time steps drifts towards the step's leading

edge. As the wave builds up over the step's edge, the flow is separated from the leading edge, forming a small negative (clockwise) vortex (Figure 9d) which keeps increasing in magnitude until $t^* = 1.0$ s (Figure 9f) at which the wave crest is located over the step's leading edge. Additionally, the positive eddy formed at the beginning of the wave progression is still propagating further downstream, forming a pair of eddies rotating in opposite directions. During this time the vorticity field between the $D/d = 0.25$ and $D/d = 0.5$ cases begins to differentiate in terms of eddy location and intensity. For example, the clockwise eddy in $D/d = 0.5$ and $D/d = 0.75$ is formed at an earlier time over the wave progression compared to the $D/d = 0.25$ step and absorbs more energy from the mean flow achieving higher vorticity magnitudes. Furthermore, the pair of eddies in the $D/d = 0.75$ case is fully separated from the step and starts moving towards the water surface (Figure 9f). This is a result of the increasing water level due to the immediate change in water depth that generates an uplift force drifting the pair of eddies upwards. In later stages, as the water level decreases, the pair of eddies are pushed downwards and a positive eddy starts to form at the step's leading edge and keeps increasing in magnitude over time (for $t^* \geq 1.4$) as a result of the negative flow imposed by the wave trough. The latter is mostly observed in the $D/d = 0.25$ and $D/d = 0.5$ cases while in the steepest case the vorticity magnitude of the positive eddy is rather decreased. This might be due to the interaction of the water surface with the leading edge and immediate change in velocity gradient at this location. During this time the negative eddy formed before is propagating upstream from the structure forming another pair of eddies rotating in opposite directions.

In Figure 10 the effect of the step's height on the vorticity magnitude as well as the evolution of vortices formed at the leading edge are better observed. First, the trend of the formation, progression and dissipation of the vortices is similar in all cases. The negative (clockwise eddy) starts to form at $t^* = 0.4$ s in all cases and reaches a maximum vorticity magnitude at $t^* = 1.0$ s at which the wave crest is exactly over the leading edge and from then it starts to dissipate until it reforms in the next wave. The magnitude of the negative eddy increases with increasing step height with a maximum magnitude of $\omega_{Y_{\max}} = 60 \text{ s}^{-1}$ at $D/d = 0.75$ compared to the shallower cases where the vorticity peaks at $\omega_{Y_{\max}} = 40 \text{ s}^{-1}$ and $\omega_{Y_{\max}} = 50 \text{ s}^{-1}$, $D/d = 0.25$ and $D/d = 0.5$ respectively. In contrast to the negative vorticity, the step height seems not to have a strong effect on the positive eddy formed at the leading edge, especially in heights between $D/d = 0.25$ and $D/d = 0.5$. Nevertheless, in the case of $D/d = 0.75$ the positive eddy peaks at $\omega_{Y_{\max}} = 30 \text{ s}^{-1}$ whereas in the other two cases at around $\omega_{Y_{\max}} = 40 \text{ s}^{-1}$; however, at different times during a wave progression.

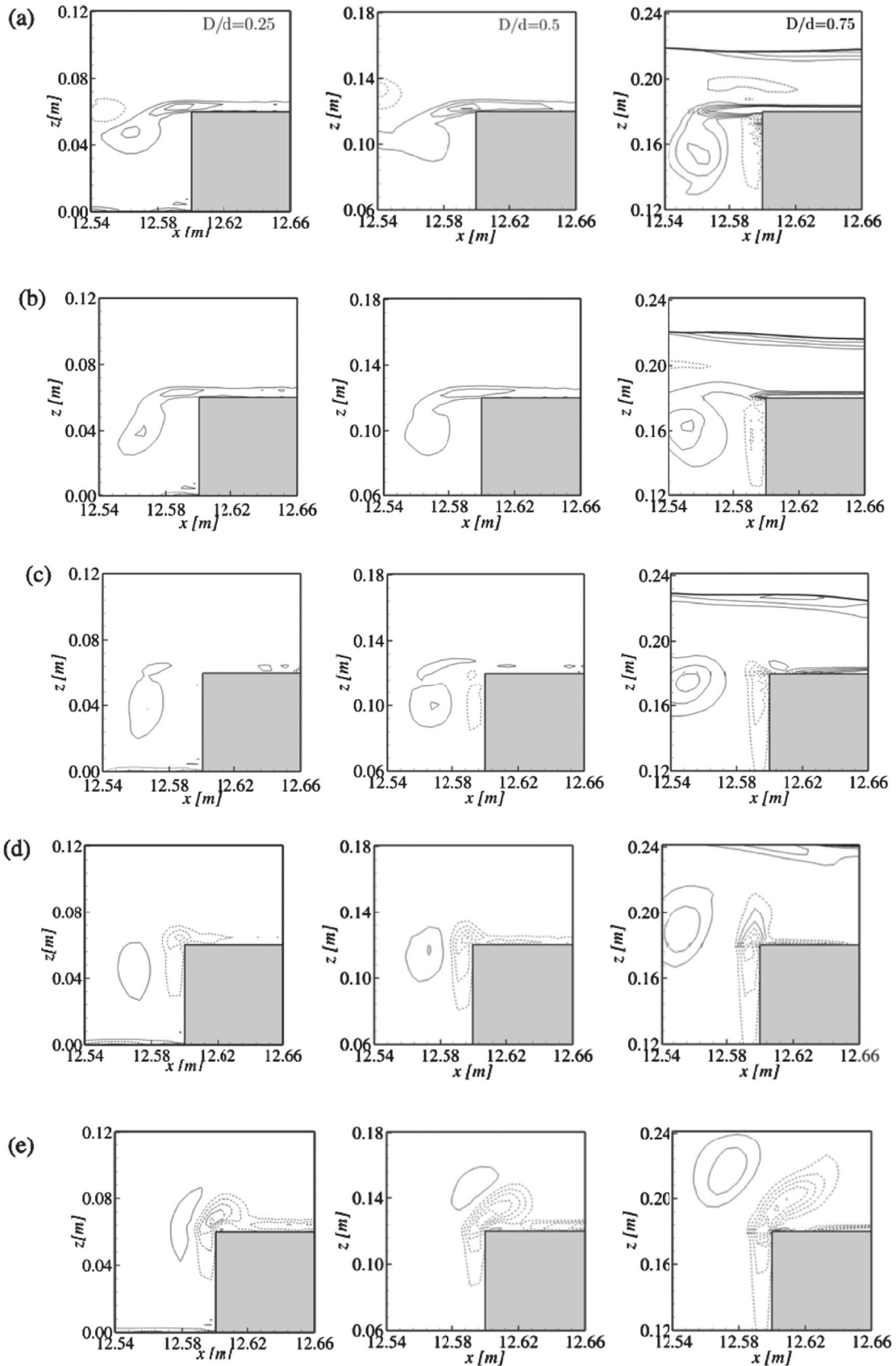


Figure 9. Vorticity field evolution near the leading edge over one wave period as shown in Figure 8 plotted every $\Delta t = 0.2$ s for $D/d = 0.25$ (left), $D/d = 0.5$ (middle) and $D/d = 0.75$ (right). Solid lines represent counterclockwise and dashed lines clockwise vorticity. Screenshots are plotted every $\Delta t = 0.2$ s. (a)–(j) $t^* = 0.0$ s to $t^* = 1.8$ s.

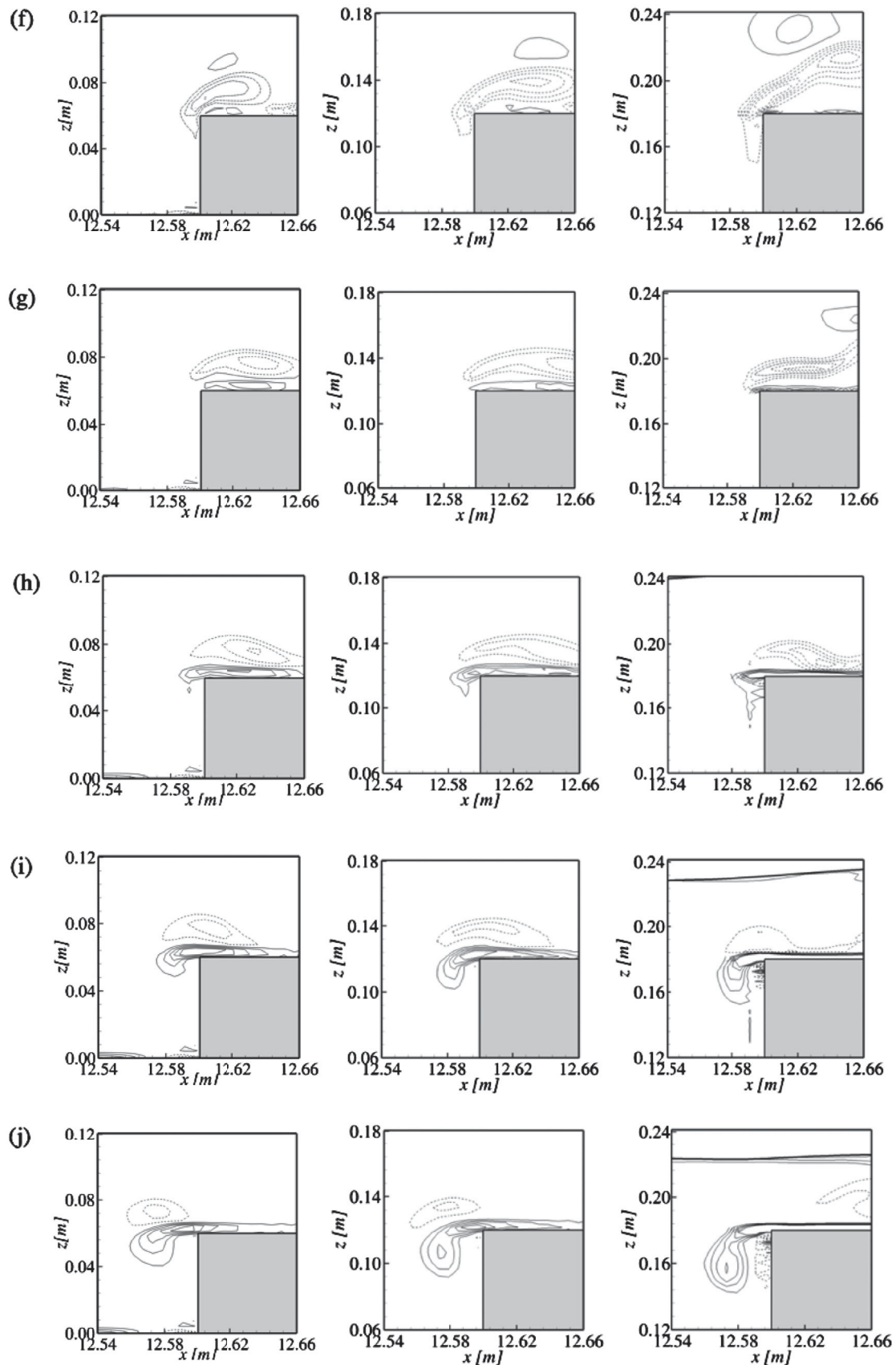


Figure 9. Continued.

Trailing edge

Figures 11–13 plot the water surface elevation over the trailing edge, the vorticity field and vorticity magnitude, respectively. In Figure 11 the water surface as

recorded at the step's trailing edge is plotted from a wave probe introduced at $D/d = 0.5$ for supporting the discussion on the effect of wave elevation on the trailing edge eddy formation. Figure 12 plots the vorticity field

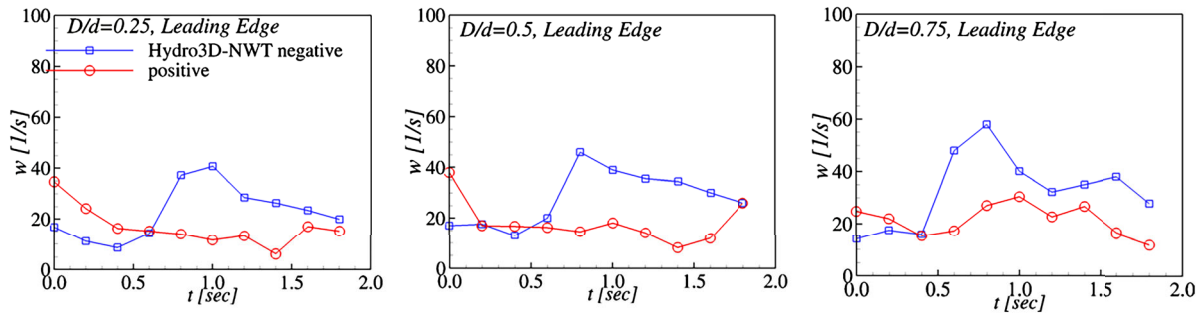


Figure 10. Maximum vorticity magnitude recorded near the leading edge for $D/d = 0.25$ (left), $D/d = 0.5$ (middle) and $D/d = 0.75$ (right) over one wave period.

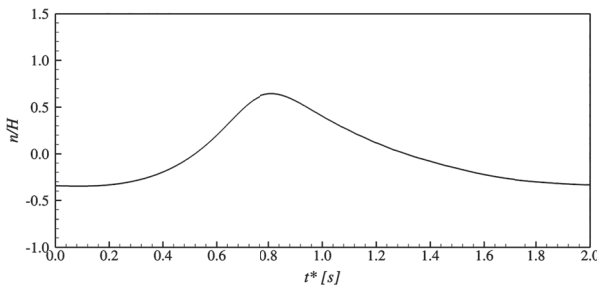


Figure 11. Wave elevation over the trailing edge ($x = 13.0$ m) where $t^* = 0.0$ s is set at when $t = 22.45$ s.

near the step's trailing edge for $D/d = 0.25$ (left panel), $D/d = 0.5$ (centre panel) and $D/d = 0.75$ (right panel) every $\Delta t = 0.2$ s over the last wave period simulated by the current code. For visualization purposes, the initial time $t^* = 0.0$ s is related to $t = 22.45$ s. In contrast to the near-leading edge vorticity field, the step height has a dominant effect on the vorticity intensity and vortex formation. In the shallower cases ($D/d = 0.25$ and $D/d = 0.5$) a very similar vorticity field in terms of vortex shedding time and location is observed however the vorticity magnitude varies through the wave progression. On the other hand, the vorticity field on the $D/d = 0.75$ step's trailing edge demonstrates a unique progression that varies between the other two cases. Large energetic eddies are formed near the trailing edge first due to the higher velocity levels formed at shallower water depths as well as the increased velocities over the structure moments before and after wave breaking.

In Figure 12a, a pair of eddies rotating at opposite directions formed at earlier time steps due to the action of the previous wave are located over the step near the trailing edge. In $D/d = 0.25$ and $D/d = 0.5$ cases, the location of the eddies is similar; however, in the latter, their size as well as their magnitude are greater due to higher velocities at $D/d = 0.5$ step's edge. Considering the steepest case ($D/d = 0.75$) at the same time instance, a strong single positive eddy is formed evidently at a later stage compared to the shallower step heights. Additionally, the opposite pair eddy is located at a deeper water depth. In this case, the decreased water surface level and the finite distance from the step's upper surface to the water level have a major effect

on the eddy shape, location and intensity. At $t^* = 0.2$ s (Figure 12b) the positive (counterclockwise) vortex in the case of the first two step heights drifts upwards and towards the leading edge with decreasing vortex intensity due to the progression of the wave crest over the submerged structure, whereas the eddy formed at the $D/d = 0.75$ is still growing but fixed at the step's upper surface due to the downward force acting by the reduced water level. From $t^* = 0.4$ s onwards the wave crest approaches the step's trailing forming a positive flow (from left to right), shifting the vortices formed earlier downstream from the structure. In Figure 12d a clockwise (negative) eddy starts to form due to flow separation at the step's trailing edge and the positive horizontal velocity imposed by the wave progression, forming a pair of eddies rotating in opposite directions, drifting further downstream following the wave motion. From $t^* = 0.8$ s the negative vortex vorticity magnitude increases similarly in all cases; however, a more unique interaction between the rotational flow structures and the water surface is observed in the $D/d = 0.75$ case. For example, in Figure 12f the location and overall vorticity field are very similar in the first two cases ($D/d = 0.25$ and $D/d = 0.5$) whereas a clearly more energetic negative eddy is formed strongly interacting with the previously formed positive eddy. In this instance, the sharp wave crest formed moments before breaking generates a nonlinear interaction of the flow below the water surface, re-forming the vorticity field, generating strong wave-induced flow eddy interactions. As a result, smaller secondary eddies are generated at later time steps (Figure 12g, h), whereas a less turbulent vorticity field is observed in the $D/d = 0.25$ and $D/d = 0.5$ cases. From $1.4 \text{ s} \leq t^* \leq 1.8 \text{ s}$ the negative flow imposed by the wave trough approaching the step's leading edge generates a positive eddy drifting from the lower downstream edge to the upper surface of the structure. Similar to earlier time steps, the vortex shedding in the steepest structure occurs at later stages during the wave propagation due to the interaction of the water surface with the submerged eddies and the finite distance from the step edge to the water level.

Figure 13 plots the maximum vorticity magnitude of the negative (blue lines) and positive (red lines)

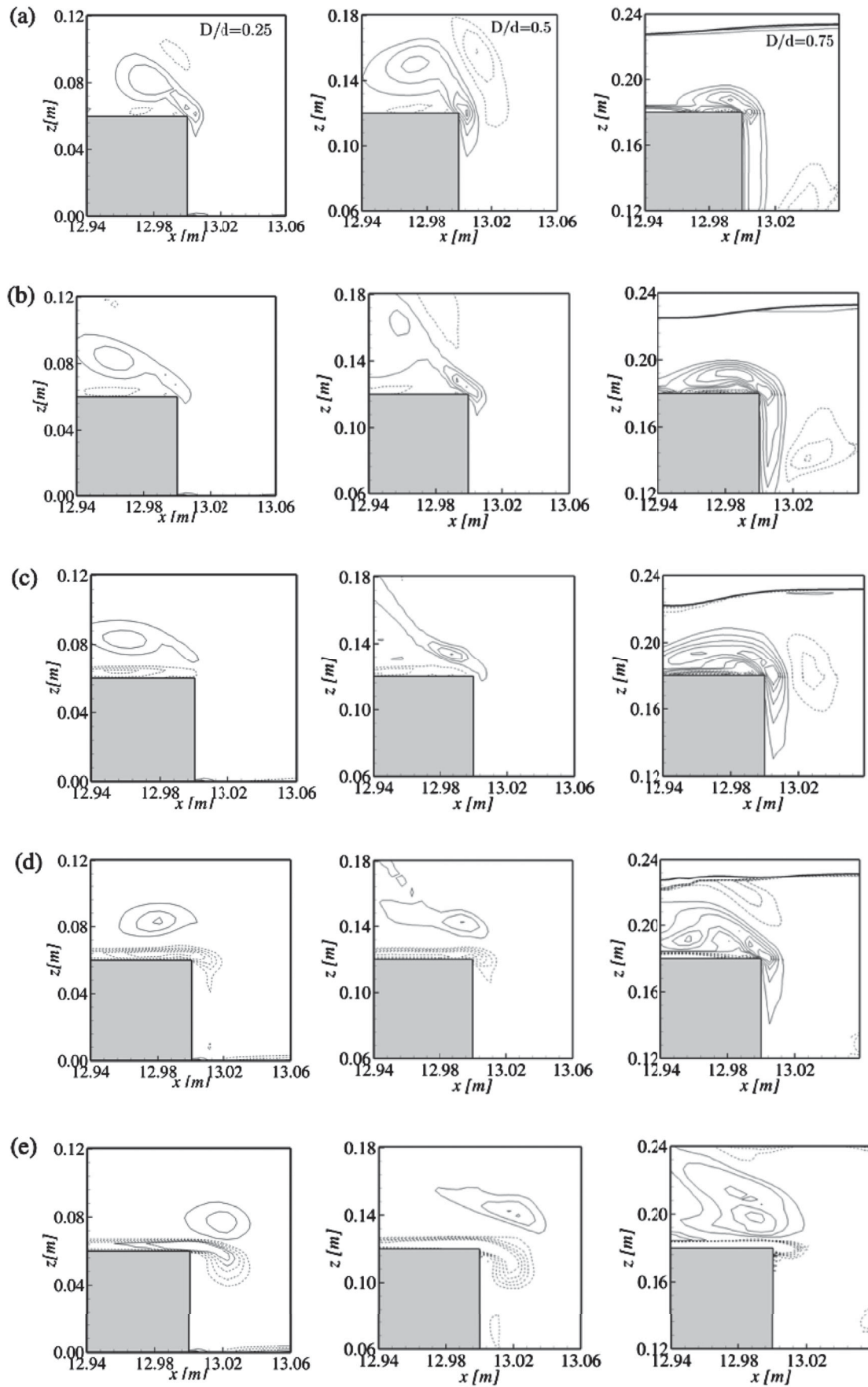


Figure 12. Vorticity field evolution near the trailing edge over one wave period as shown in Figure 11 plotted every $\Delta t = 0.2$ s for $D/d = 0.25$ (left), $D/d = 0.5$ (middle) and $D/d = 0.75$ (right). Solid lines represent counterclockwise and dashed lines clockwise vorticity. Screenshots are plotted every $\Delta t = 0.2$ s. (a)–(j) $t^* = 0.0$ s to $t^* = 1.8$ s.

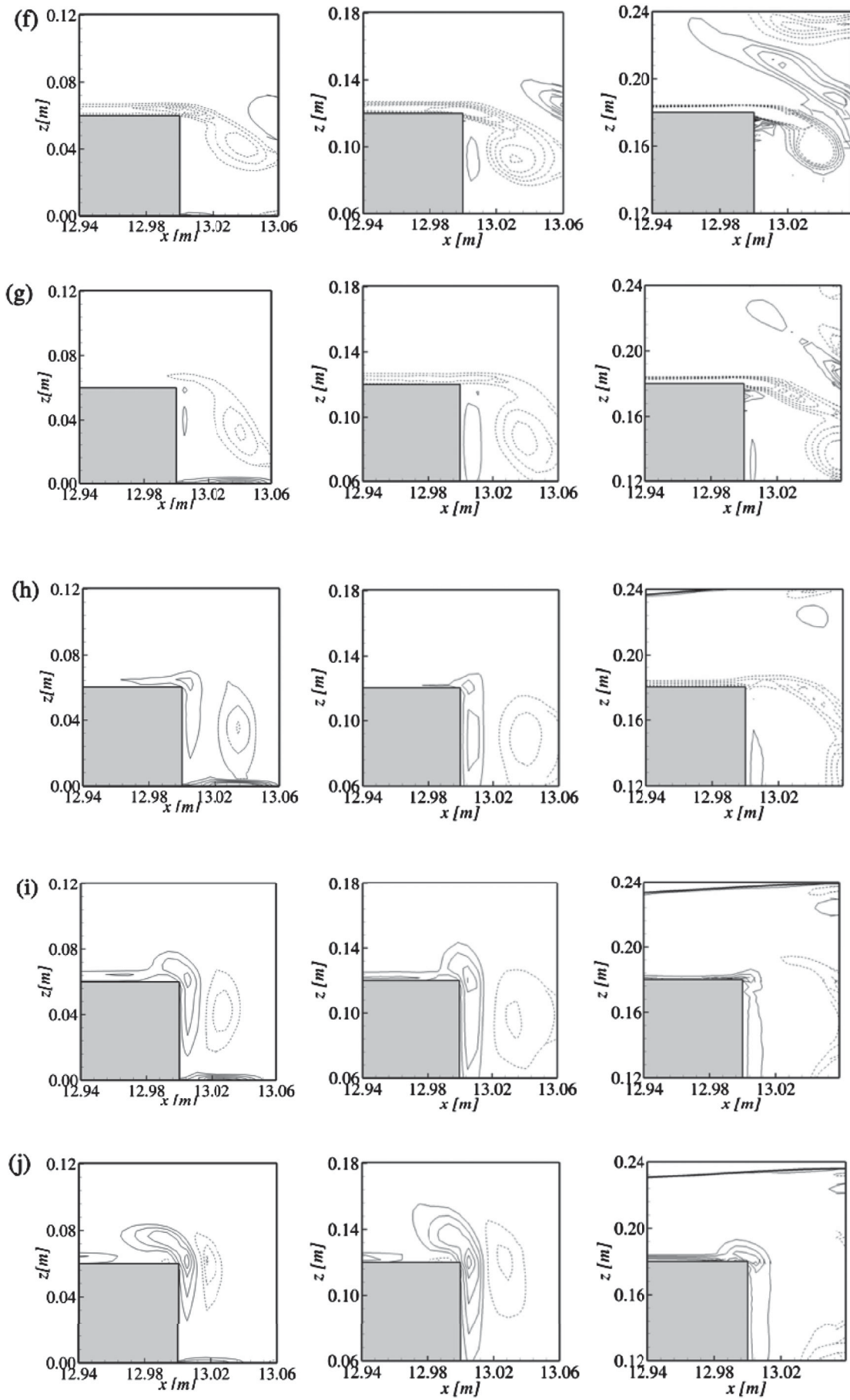


Figure 12. Continued.

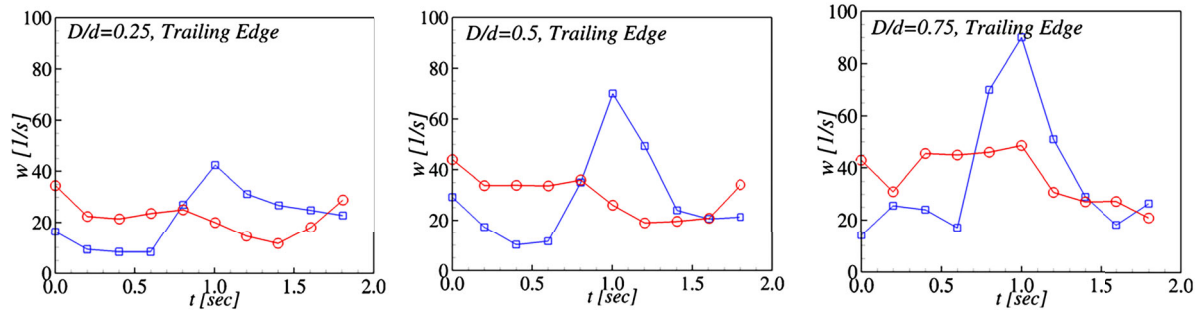


Figure 13. Maximum vorticity magnitude recorded near the trailing edge for $D/d = 0.25$ (left), $D/d = 0.5$ (middle) and $D/d = 0.75$ (right) over one wave period.

eddies corresponding to the screenshots of the vorticity field presented in Figure 12. In all cases, the evolution of the negative vortex formed at the step's trailing edge follows a similar trend. This clockwise eddy is generated at $t^* = 0.6$ s at which the wave crest approaches the step's edge and the water level starts to build up, generating a positive flow. The vorticity magnitude increases until it reaches a maximum value at $t^* = 1.0$ s in all cases, at which the wave crest is located over the trailing edge generating maximum wave-induced velocity. After that time the negative eddy starts to fade before it re-forms in the following wave. Nevertheless, the step height clearly affects the peak of the maximum vorticity of the clockwise eddy which peaks at $\omega_{Y_{\max}} = 45 \text{ s}^{-1}$, $\omega_{Y_{\max}} = 70 \text{ s}^{-1}$ and $\omega_{Y_{\max}} = 95 \text{ s}^{-1}$ at $D/d = 0.25$, $D/d = 0.5$ and $D/d = 0.75$, respectively. Overall the clockwise eddy reaches higher vorticity magnitudes at the trailing edge compared to the leading edge (Figure 10). Considering the positive eddy which is formed on the upper surface of the trailing edge due to the negative flow imposed from the wave trough, the maximum vorticity magnitude peaks at lower levels compared to the negative eddy but increases with increasing step height, $\omega_{Y_{\max}} = 38 \text{ s}^{-1}$, $\omega_{Y_{\max}} = 45 \text{ s}^{-1}$ and $\omega_{Y_{\max}} = 50 \text{ s}^{-1}$ at $D/d = 0.25$, $D/d = 0.5$ and $D/d = 0.75$, respectively. However, the positive vortex shedding does not follow the same trend as the negative eddy and is characterized by a smooth evolution. This is a result of the quick change of the flow direction due to the wave progression and the increasing horizontal velocity over the step.

3.6. 3D vortical structures

Figure 14 demonstrates the formation of turbulent rotational flow structures near the submerged step's leading and trailing edge, based on iso-surfaces of the Q-criterion at $Q = 60$ coloured with y vorticity (ω_Y) together with the progression of the water surface based on iso-surfaces at $\phi = 0$. Here the vorticity field is plotted every $\Delta t = 0.2$ s starting from $t^* = 0.0$ s at $t = 22.05$ s (Figure 8) and comparisons are made between $D/d = 0.5$ (left panel) and $D/d = 0.75$ (right

panel) cases. The vortex shedding and vorticity field evolution plotted in this figure further supports the effect of the step's height in eddy formation, turbulent vorticity field and nonlinearity in the interaction between the rotational flow structures and the water surface, especially in $D/d = 0.5$ and $D/d = 0.75$ cases.

In both cases, the vortical structures have a similar pattern in terms of the formation and evolution of the three-dimensional rotational flow structures. However, the eddies' length scale, rotational magnitude and three dimensionality are some of the flow characteristics that differentiate the two cases. For example, at $t^* = 0.0$ s (Figure 14a), a smooth and continuous over the spanwise direction (inside the page) pair of opposite rotational eddies are formed near the $D/d = 0.5$ step's leading edge, whereas an unsteady and discontinuous in the spanwise direction pair of eddies is observed in the $D/d = 0.75$ case. A larger length scale and higher magnitude vortical structures are formed in the steepest case in both the leading and trailing edges. This is a result of two main flow characteristics, first higher velocities generated at shallower water depths based on cnoidal wave theory, and second due to the reduced distance between the water surface and the step's upper area. In the latter, as the wave approaches the step and due to the immediate reduction in the effective water depth the flow accelerates over the submergence step forming a more energetic and random vorticity structure throughout the wave progression in the steepest case ($D/d = 0.75$).

At later time instances, from $0.2 \leq t^* \leq 0.6$, the trailing edge vortical structures drift towards the structure's upper surface due to the wave-imposed negative velocity forming a new positive eddy. During this time, the vorticity field at the trailing edge of the $D/d = 0.75$ case reforms into a more random and complex progression inside which several smaller streamwise rotational flow structures rotating over the x -axis extending from the floor bed to the structure's edge are generated. These streak vortices are mixed with the main vortical structures following a similar rotation. A similar trend is observed in the $D/d = 0.5$ case; however, in less energetic levels. Considering the steps' leading edge at Figure 14b–d in both cases, the vortex structure

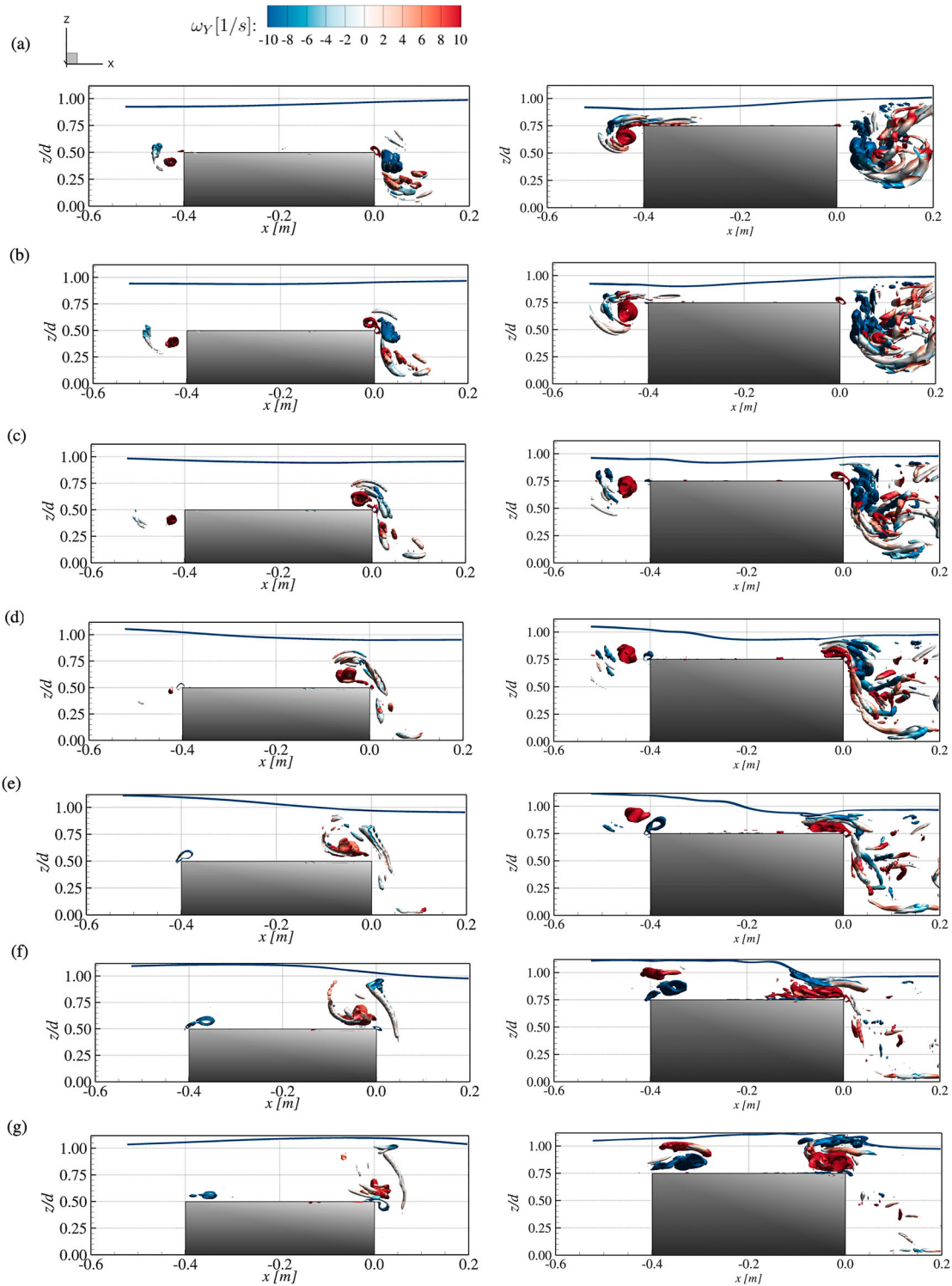


Figure 14. A side view of the three dimensional vortical structures based on the iso-surfaces of Q criterion at $Q = 60$ plotted with the water surface every $\Delta t = 0.2$ s coloured with y vorticity with $t^* = 0.0$ s set at $t = 22.05$ s for $D/d = 0.5$ (left panel) and $D/d = 0.75$ (right panel). Screenshots are plotted every $\Delta t = 0.2$ s. (a)–(j) $t^* = 0.0$ s to $t^* = 1.8$ s and the last two figures show the three-dimensional view of the two cases at $t^* = 1.8$ s.

exhibits a three dimensionality effect but at lower levels compared to the trailing edge. Nevertheless, similar to the trailing edge, streamwise or spanwise vortices rotating in x - or z -direction are formed drifting with the main positive eddy. However, in the $D/d = 0.75$ case, a larger positive eddy is formed compared to the $D/d = 0.5$ case which is followed by smaller discontinuous secondary eddies which dissipate at later stages. For

example at $t^* = 0.6$ s the positive eddy in $D/d = 0.5$ has already dissipated whereas in the $D/d = 0.75$ case, this happens at $t^* = 1.2$ s.

What follows later, Figure 14e–h, is a wave build-up over the step's upper surface leading to the formation of negative and positive eddies at the leading and trailing edge, respectively and wave breaking in the case of $D/d = 0.75$. Considering the intermediate height

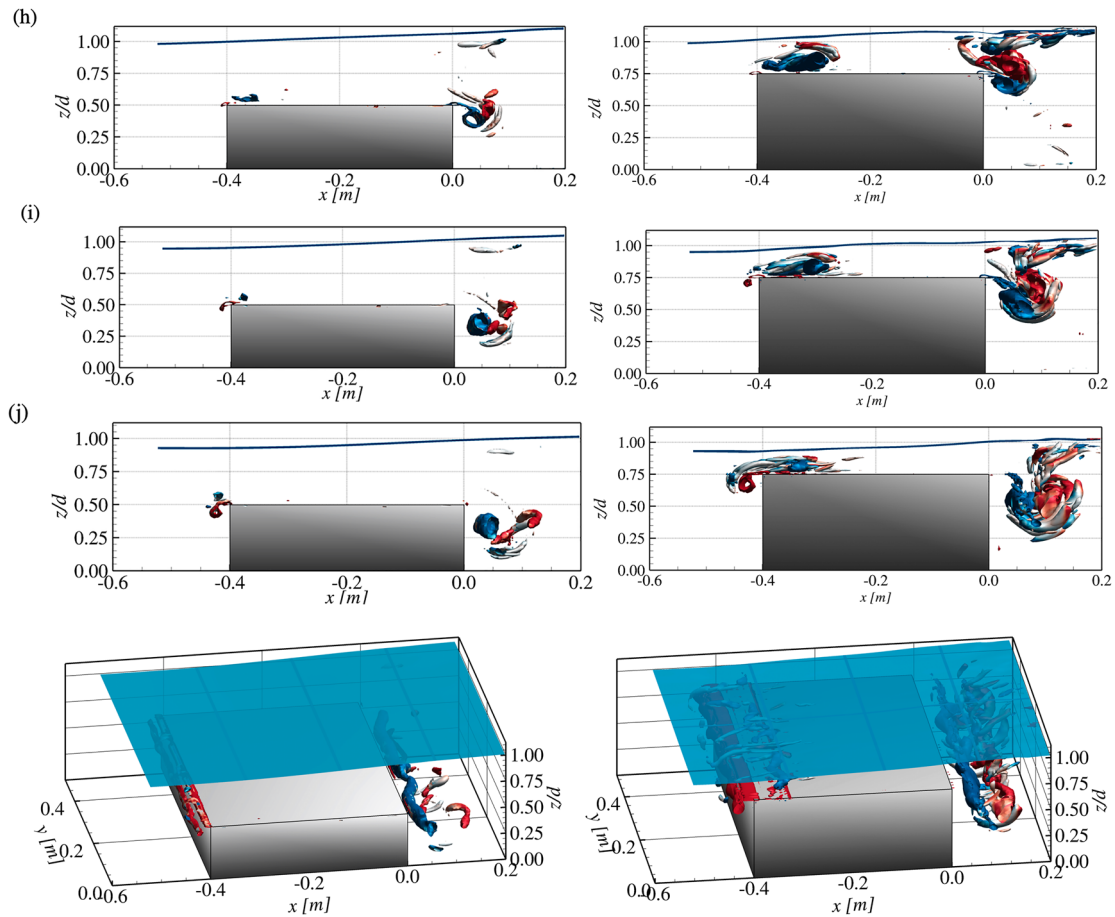


Figure 14. Continued.

case ($D/d = 0.5$), in the vicinity of the continuous positive eddy formed at earlier stages near the trailing edge, smaller billows with zero y -vorticity are formed extending from the floor bed drifting towards the water surface as the negative eddy is formed and the wave builds up over the step's trailing edge. In the case of $D/d = 0.75$, the negative flow imposed by the wave motion over the step as well as the reduced water level drifts the vortical structures formed at earlier stages on top of the step while a positive eddy is formed at the trailing edge as the wave builds up moments before breaking. Similar to $D/d = 0.5$, small billows with zero y -vorticity stretching in the stream-wise direction drift from the floor bed towards the step's upper surface. At Figure 14f, g the wave crest is located over the submerged step which is the instance at which the distance between the leading's negative and trailing's positive eddies is the shortest but no interaction of the two is observed due to the relatively large step's length compared to the wave length. From there and considering the $D/d = 0.75$ case the vortical structure oscillates with the water surface (at $t^* = 1.2$ s and $t^* = 1.4$ s) while a negative eddy is formed at the trailing edge moving further downstream together with the positive eddy formed earlier, followed by an upward motion while wave breaks on top.

In general, Figure 14 demonstrates the three dimensionality in the formation and evolution of the vortical structures as well as the effect of step height and water surface on the imposed turbulent flow field. Leading and trailing edge eddies are formed due to flow separation oscillating from the step's lateral edges towards the upper surface and vice versa due to wave progression over the step. More complex and energetic eddies are observed in the steepest case $D/d = 0.75$ with a large eddy extending throughout the width of the tank interrupted by billow eddies stretched over the stream-wise direction with zero y -vorticity extending from the floor bed to the water surface. Due to deeper submergence depths in the $D/d = 0.5$ case, the interaction of eddies formed during wave progression with the water surface is negligible whereas in the $D/d = 0.75$ a strong interaction of the vortical flow structures with the water surface is observed first from the eddies to the water surface, followed by a strong effect of the water surface on the submerged rotational flow structures at which vorticity magnitude and eddies size increases due to energy transition through wave breaking.

Figures 15 and 16 show a 3D projection of the eddy formation at $t^* = 0.8$ s and $t^* = 1.8$ s during half wave period interval, respectively near the leading (left panel) and trailing edge (right panel) for the three cases considered in this study, $D/d = 0.25$, $D/d = 0.5$ and

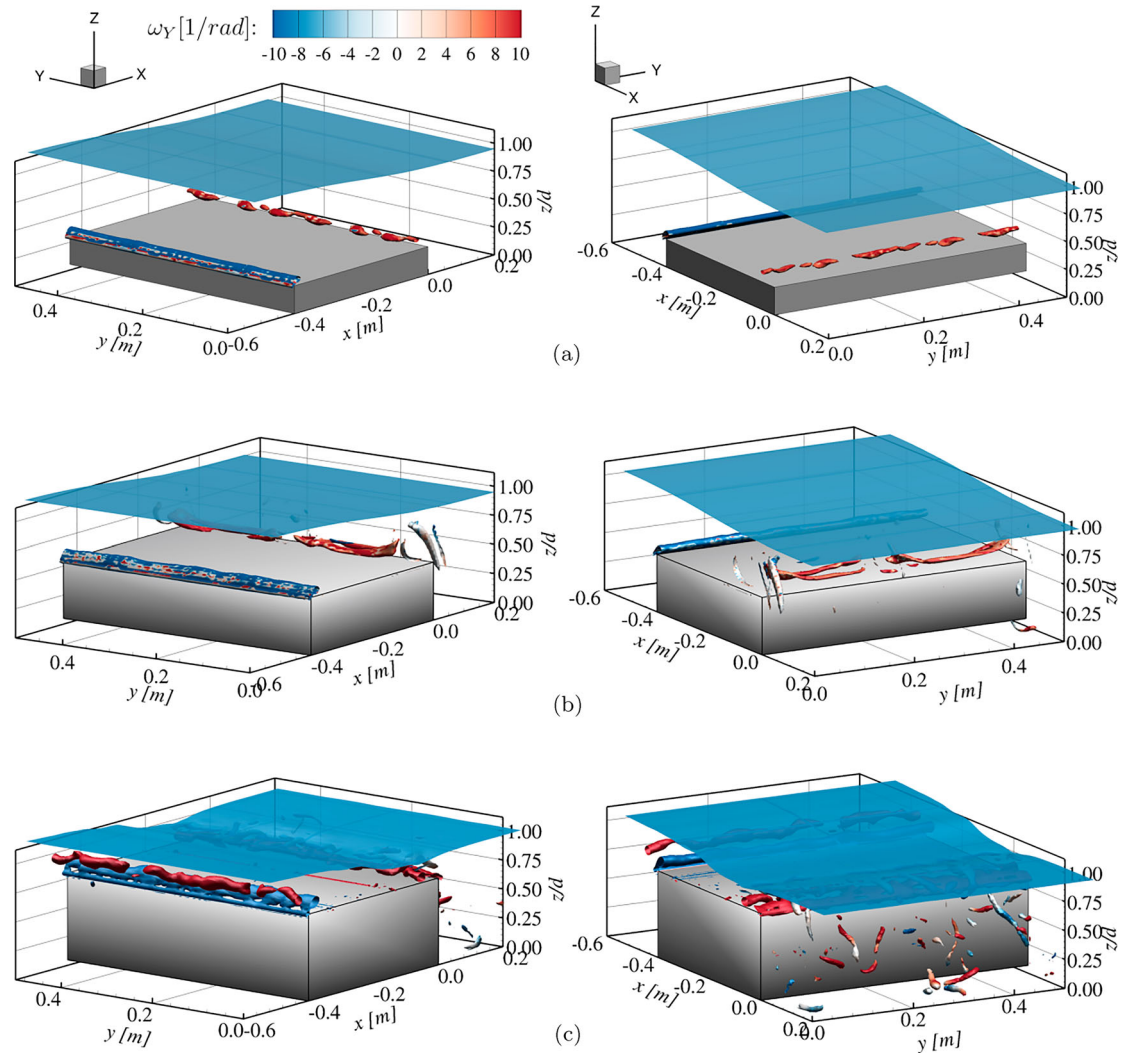


Figure 15. A leading edge (left) and a trailing edge (right) projection of the three dimensional vortical structures based on the iso-surfaces of Q criterion at $Q = 60$ plotted with the water surface at $t^* = 0.8$ s at (a) $D/d = 0.25$, (b) $D/d = 0.5$ and (c) $D/d = 0.75$ with $t^* = 0.0$ s set at $t = 22.05$ s.

$D/d = 0.75$. Evidently, with increasing step height, the intensity of rotational flow structures and the formation of random three-dimensional vortices becomes more dominant. At $t^* = 0.8$ s (Figure 15), the wave propagation over the submerged structure imposes a positive (left to right) flow over the leading edge whereas a negative flow (from right to left) is formed at the trailing edge's location. As a result, a dominant clockwise eddy is formed over the leading edge observed in all three step heights. However, in the case of $D/d = 0.75$ (Figure 15b) the vortical flow structures near the leading edge are evidently different from the other two and a counterclockwise eddy is also presented with the clockwise eddy formed at a previous time instance as a result of the shallow water depth between the step and the water surface. At the trailing edge's location, a counterclockwise eddy is formed similarly in all step heights and as expected the intensity of the rotational flow structure increases with increasing step height. In the case of $D/d = 0.75$ the flow field near the leading edge is characterized by random and energetic secondary

vortices due to wave breaking and increased turbulence intensity at this location.

At a late stage (Figure 16) and considering $D/d = 0.25$ (Figure 16a), the rotational flow structures both in the leading and trailing edges are smooth and continuous throughout the width of the domain while the three dimensionality in the vortical structures is almost negligible. At $D/d = 0.5$ (Figure 16b), the eddies are affected by three-dimensional effects with small finite rotational structures which interrupt the continuous distribution of the main eddies in the leading and trailing edges. At this time instance, the trailing edge negative (clockwise) eddy is clearly more affected by three-dimensional effects compared to the leading edge eddy which is the case in all step heights due to the higher velocities formed over the step and close to the trailing edge. In Figure 16c the relatively large step height generates strong wave-structure interactions resulting in dominant rotational eddies both in leading and trailing edge. In this instance, an energetic positive eddy is located near the leading edge

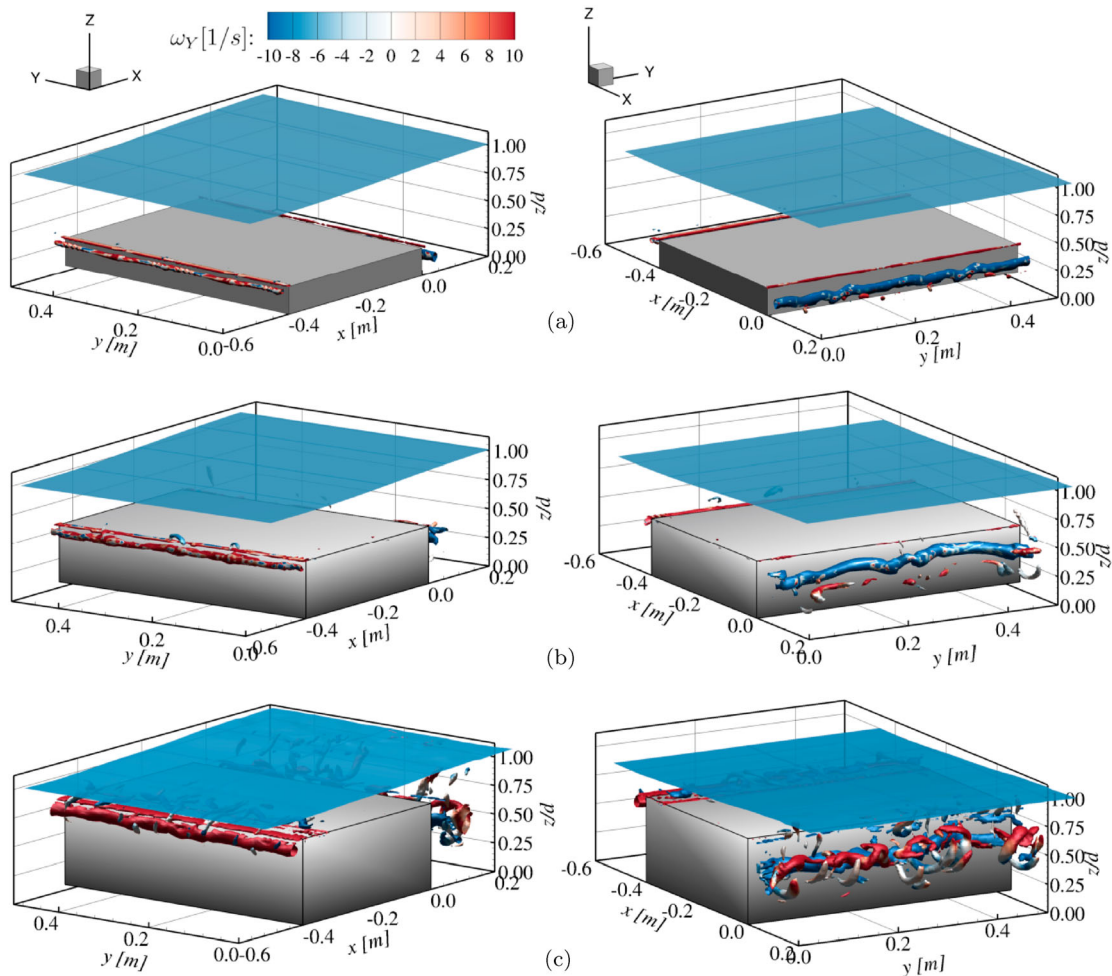


Figure 16. A leading edge (left) and a trailing edge (right) projection of the three dimensional vortical structures based on the iso-surfaces of Q criterion at $Q = 60$ plotted with the water surface at $t^* = 1.8$ s at (a) $D/d = 0.25$, (b) $D/d = 0.5$ and (c) $D/d = 0.75$ with $t^* = 0.0$ s set at $t = 22.05$ s.

extending throughout the full width of the domain accompanied by small streamlined eddies with zero y -vorticity whereas a much more turbulent eddy field is formed at the trailing edge at which the main clockwise rotational eddy is completely interrupted by secondary eddies rotating in various directions as a result of the high velocities and the blend effect occurred from wave breaking.

4. Conclusions

In this study, the LES based numerical wave tank, Hydro3D-NWT, has been employed to simulate periodic waves propagating over a submerged step in shallow water depths and investigate the effect of various step heights on local hydrodynamic characteristics. To study the effect of various step heights, a previously conducted experiment has been reproduced to examine first the accuracy of the code in predicting accurate wave–structure interactions. Results of wave elevations as well as maximum vorticity magnitudes suggest that Hydro3D-NWT can generate accurate wave–structure interaction and accurately reproduce the near-structure flow evolution. In this study three step heights have

been considered, a shallow, an intermediate and a steep submerged step, with step height to water depth ratio (D/d) of 0.25, 0.5 and 0.75 respectively, all under the same wave conditions. Conclusions are made based on plots of water surface fluctuations, vorticity fields as well as snapshots of three-dimensional vortical structures. As expected, the effect of the submerged structure on the water surface increases with increasing step height. Considering the $D/d = 0.25$ case, results have shown that the water surface remains unchanged both upstream and downstream from the structure whereas a wave breaking and large wave reflections propagating in all directions inside the tank were observed in the case of $D/d = 0.75$. In the intermediate step height ($D/d = 0.5$) the wave elevations varied near the structure as a result of the immediate change in water depth without wave breaking occurring. The vorticity field has been examined at both step's leading and trailing edge in terms of the maximum vorticity magnitude of the negative (clockwise) and positive (counterclockwise) spanwise eddy. Considering the leading edge, the formation, progression and dissipation of both positive and negative eddies have shown a similar trend; however, the step's height was found to have a more

direct effect on the vorticity magnitude of the negative eddy with values of vorticity magnitude increasing with increasing step height. On the other hand, the maximum values of vorticity magnitude of the positive eddy were found to increase with increasing step height but not at the same rate as in the negative eddy vorticity. Positive and negative eddies formed on the step's trailing edge were found to have a similar progression as the ones generated at the leading edge; however, the effect of step height was found to be greater and both positive and negative eddies were characterized by higher vorticity magnitudes.

Additionally, results of three-dimensional vortical structures near the leading and trailing edges have demonstrated the effect of step height on the formation of strong dominant turbulent flow structures. Except for the $D/d = 0.25$ case, strong energetic eddies extending through the total width of the domain were formed near the intermediate and steep submerged step surrounded by three-dimensional rotational billow flow structure with zero y vorticity interrupting the uniformity of the primary eddies. As expected the increasing velocities presented in the steepest case as well as the very finite distance of the step's upper surface to the water surface resulted in dominant energetic eddies which were deformed by the progression of waves on the top.

The numerical simulations and results presented in this study highlighted the complex flow dynamics involved in these applications that can be used to adopt better engineering approaches to design more efficient submerged breakwaters, understanding the importance of submerged breakwaters' location and relevant water depth to step height ratio and utilize the developed flow field for retrofitting wave energy converters. In the present study, only one set of wave parameters was employed from the experiments to conduct these simulations and therefore the effect of the ratio of wavelength to submerged step's length was not under study. This ratio is expected to have a major impact on the near-structure flow field and vortex shedding and will be examined in future research activities. Additional future activities include the investigation of various vertical location of a rectangular box. For example, cases of fully submerged, partially submerged or fully exposed rectangular structures will be included in future research to cover more realistic conditions.

Disclosure statement

No potential conflict of interest was reported by the author(s).

Funding

This work was financially supported by the Engineering and Physical Sciences Research Council (EPSRC) through grant (EP/V040235/1) and the EPSRC funding from eCSE project

(ARCHER2-eCSE11-15) via ARCHER2 service at the University of Edinburgh. Z.X. is partially supported by the Royal Society Newton Advanced Fellowship (NAF/R1/201156) and International Exchanges Award (IEC/NSFC/211143, IES/R2/202095), and the Alexander von Humboldt Research Fellowship for Experienced Researchers.

Notation

C_w	WALE constant
d	Water-depth (m)
dx, dy, dz	Grid size (m)
f	Frequency (Hz)
F_i^{sf}	Surface tension force (m/s ²)
f_i	External Force (m/s ²)
g	Air properties
g	Gravitational acceleration (m/s ²)
g_{ij}	Velocity tensor (m/s)
H	Wave-height (m)
$H(\phi)$	Heaviside function
k	Curvature (1/m)
k_{cutoff}	Filter size (m)
l	Water properties
L	Wavelength (m)
n	Wave elevation (m)
n_i	Normal unit vector
N_{tot}	Total number of grid cells
p	Pressure (N/m ²)
R	Relaxation function constant
r	Radius (m)
S_{ij}	Rate of strain tensor (1/s)
T	Wave period (s)
t	Time (s)
u_i	Velocity (m/s)
u_∞	Far field velocity (m/s)
x_i	Coordinates x, y, z (m)
$-$	Spatial filtered variables
$\delta(\phi)$	Delta function
Γ	Water-air interface
$\Gamma(x)$	Relaxation function
ν	Kinematic viscosity (m ² /s)
ν_t	Eddy viscosity (m ² /s)
ν_T	Total viscosity (m ² /s)
Ω_g	Cells occupied by air
Ω_l	Cells occupied by water
ω	Vorticity (1/s)
ϕ	Signed distance function
ρ	Density (Kg/m ³)
σ	Surface tension coefficient (N/m)
$\tau^{SGS_{ij}}$	Sub grid scale tensor
ε	Thickness size of water-air interface (m)

ORCID

Aristos Christou  <http://orcid.org/0009-0005-2116-7832>
 Thorsten Stoesser  <http://orcid.org/0000-0001-8874-9793>
 Zhihua Xie  <http://orcid.org/0000-0002-5180-8427>

References

- Agarwal, S., Sriram, V., & Murali, K. (2022). Three-dimensional coupling between Boussinesq (FEM) and Navier–Stokes (particle based) models for wave structure interaction. *Ocean Engineering*, 263, Article 112426. <https://doi.org/10.1016/J.OCEANENG.2022.112426>
- Brocchini, M., Marini, F., Postacchini, M., Zitti, G., Falchi, M., & Xie, Z. (2022). Interaction between breaking-induced vortices and nearbed structures. Part I: Experimental and theoretical investigation. *Journal of Fluid Mechanics*, 940, A44. <https://doi.org/10.1017/jfm.2022.260>
- Buldakov, E., Higuera, P., & Stagonas, D. (2019). Numerical models for evolution of extreme wave groups. *Applied Ocean Research*, 89, 128–140. <https://doi.org/10.1016/j.apor.2019.05.013>
- Cevheri, M., McSherry, R., & Stoesser, T. (2016). A local mesh refinement approach for large-eddy simulations of turbulent flows. *International Journal for Numerical Methods in Fluids*, 82(5), 261–285. <https://doi.org/10.1002/flid.4217>
- Chang, K. A., Hsu, T. J., & Liu, P. L. (2001). Vortex generation and evolution in water waves propagating over a submerged rectangular obstacle: Part I. Solitary waves. *Coastal Engineering*, 44(1), 13–36. [https://doi.org/10.1016/S0378-3839\(01\)00019-9](https://doi.org/10.1016/S0378-3839(01)00019-9)
- Chang, K. A., Hsu, T. J., & Liu, P. L. (2005). Vortex generation and evolution in water waves propagating over a submerged rectangular obstacle. Part II: Cnoidal waves. *Coastal Engineering*, 52(3), 257–283. <https://doi.org/10.1016/j.coastaleng.2004.11.006>
- Chen, L. F., Stagonas, D., Santo, H., Buldakov, E. V., Simons, R. R., Taylor, P. H., & Zang, J. (2019). Numerical modelling of interactions of waves and sheared currents with a surface piercing vertical cylinder. *Coastal Engineering*, 145, 65–83. <https://doi.org/10.1016/j.coastaleng.2019.01.001>
- Chorin, A. J. (1968). Numerical solution of the Navier–Stokes equations. *Mathematics of Computation*, 22(104), 745–745. <https://doi.org/10.1090/S0025-5718-1968-0242392-2>
- Christou, A., Stoesser, T., & Xie, Z. (2020). A solitary wave interaction with a submerged thin plate in various angles of attack. In *The 30th International Ocean and Polar Engineering Conference*. OnePetro.
- Christou, A., Stoesser, T., & Xie, Z. (2021). A large-eddy-simulation-based numerical wave tank for three-dimensional wave-structure interaction. *Computers & Fluids*, 231, Article 105179. <https://doi.org/10.1016/J.COMPFLUID.2021.105179>
- Christou, A., Xie, Z., Stoesser, T., & Ouro, P. (2021). Propagation of a solitary wave over a finite submerged thin plate. *Applied Ocean Research*, 106, Article 102425. <https://doi.org/10.1016/j.apor.2020.102425>
- Christou, M., Swan, C., & Gudmestad, O. T. (2008). The interaction of surface water waves with submerged breakwaters. *Coastal Engineering*, 55(12), 945–958. <https://doi.org/10.1016/j.coastaleng.2008.02.014>
- Chu, C. R., Huynh, L. E., & Wu, T. R. (2022). Large eddy simulation of the wave loads on submerged rectangular decks. *Applied Ocean Research*, 120, 103051. <https://doi.org/10.1016/J.APOR.2022.103051>
- Fraga, B., Stoesser, T., Lai, C. C., & Socolofsky, S. A. (2016). A LES-based Eulerian-Lagrangian approach to predict the dynamics of bubble plumes. *Ocean Modelling*, 97, 27–36. <https://doi.org/10.1016/j.ocemod.2015.11.005>
- Hsu, T., Hsieh, C. M., & Hwang, R. R. (2004). Using RANS to simulate vortex generation and dissipation around impermeable submerged double breakwaters. *Coastal Engineering*, 51, 557–579. <https://doi.org/10.1016/j.coastaleng.2004.06.003>
- Hur, D. S., Lee, W. D., & Cho, W. C. (2012). Three-dimensional flow characteristics around permeable submerged breakwaters with open inlet. *Ocean Engineering*, 44, 100–116. <https://doi.org/10.1016/J.OCEANENG.2012.01.029>
- Kramer, M., Zanuttigh, B., Van der Meer, J., Vidal, C., & Gironella, F. (2005). Laboratory experiments on low-crested breakwaters. *Coastal Engineering*, 52(10–11), 867–885. <https://doi.org/10.1016/j.coastaleng.2005.09.002>
- Lara, J. L., Losada, I. J., & Guanache, R. (2008). Wave interaction with low-mound breakwaters using a RANS model. *Ocean Engineering*, 35(13), 1388–1400. <https://doi.org/10.1016/J.OCEANENG.2008.05.006>
- Lin, M., & Huang, L. (2010). Vortex shedding from a submerged rectangular obstacle attacked by a solitary wave. *Journal of Fluid Mechanics*, 651, 503–518. <https://doi.org/10.1017/S0022112010000145>
- Lin, M. Y., & Huang, L. H. (2009). Study of water waves with submerged obstacles using a vortex method with Helmholtz decomposition. *International Journal for Numerical Methods in Fluids*, 60(2), 119–148. <https://doi.org/10.1002/flid.v60:2>
- Lin, P. (2004). A numerical study of solitary wave interaction with rectangular obstacles. *Coastal Engineering*, 51(1), 35–51. <https://doi.org/10.1016/j.coastaleng.2003.11.005>
- Liu, C., Huang, Z., & Keat Tan, S. (2009). Nonlinear scattering of non-breaking waves by a submerged horizontal plate: Experiments and simulations. *Ocean Engineering*, 36(17–18), 1332–1345. <https://doi.org/10.1016/j.oceaneng.2009.09.001>
- Liu, Z., & Wang, Y. (2020). Numerical investigations and optimizations of typical submerged box-type floating breakwaters using SPH. *Ocean Engineering*, 209, Article 107475. <https://doi.org/10.1016/J.OCEANENG.2020.107475>
- Martins, G. M., Amaral, A. F., Wallenstein, F. M., & Neto, A. I. (2009). Influence of a breakwater on nearby rocky intertidal community structure. *Marine Environmental Research*, 67(4–5), 237–245. <https://doi.org/10.1016/j.marenvres.2009.03.002>
- Mayer, S., Garapon, A., & Sørensen, L. S. (1998). A fractional step method for unsteady free-surface flow with applications to non-linear wave dynamics. *International Journal for Numerical Methods in Fluids*, 28(2), 293–315. [https://doi.org/10.1002/\(SICI\)1097-0363\(19980815\)28:2<293::AID-FLD719>3.0.CO;2-1](https://doi.org/10.1002/(SICI)1097-0363(19980815)28:2<293::AID-FLD719>3.0.CO;2-1)
- Mostert, W., Popinet, S., & Deike, L. (2022). High-resolution direct simulation of deep water breaking waves: Transition to turbulence, bubbles and droplets production. *Journal of Fluid Mechanics*, 942, A27. <https://doi.org/10.1017/jfm.2022.330>
- Nicoud, F., & Ducros, F. (1999). Subgrid-scale stress modelling based on the square of the velocity gradient tensor. *Flow, Turbulence and Combustion*, 62(3), 183–200. <https://doi.org/10.1023/A:1009995426001>
- Ning, D. Z., Teng, B., Eatock Taylor, R., & Zang, J. (2008). Numerical simulation of non-linear regular and focused waves in an infinite water-depth. *Ocean Engineering*, 35, 887–899. <https://doi.org/10.1016/j.oceaneng.2008.01.015>
- Osher, S., & Sethian, J. A. (1988). Fronts propagating with curvature-dependent speed: Algorithms based on Hamilton–Jacobi formulations. *Journal of Computational Physics*, 79(1), 12–49. [https://doi.org/10.1016/0021-9991\(88\)90002-2](https://doi.org/10.1016/0021-9991(88)90002-2)

- Stoesser, T., McSherry, R., & Fraga, B. (2015). Secondary currents and turbulence over a non-uniformly roughened open-channel bed. *Water*, 7(12), 4896–4913. <https://doi.org/10.3390/w7094896>
- Sussman, M., Smereka, P., & Osher, S. (1994). A level set approach for computing solutions to incompressible two-phase flow. *Journal of Computational Physics*, 114(1), 146–159. <https://doi.org/10.1006/jcph.1994.1155>
- Ting, C. L., Chao, W. T., & Young, C. C. (2016). Experimental investigation of nonlinear regular wave transformation over a submerged step: Harmonic generation and wave height modulation. *Coastal Engineering*, 117, 19–31. <https://doi.org/10.1016/j.coastaleng.2016.07.005>
- Tripepi, G., Aristodemo, F., Meringolo, D. D., Gurnari, L., & Filianoti, P. (2020). Hydrodynamic forces induced by a solitary wave interacting with a submerged square barrier: Physical tests and δ -LES-SPH simulations. *Coastal Engineering*, 158, 103690. <https://doi.org/10.1016/j.coastaleng.2020.103690>
- Uhlmann, M. (2005). An immersed boundary method with direct forcing for the simulation of particulate flows. *Journal of Computational Physics*, 209(2), 448–476. <https://doi.org/10.1016/j.jcp.2005.03.017>
- Wiegel, R. L. (1960). A presentation of cnoidal wave theory for practical application. *Journal of Fluid Mechanics*, 7(2), 273–286. <https://doi.org/10.1017/S0022112060001481>
- Xie, Z., Stoesser, T., Yan, S., Ma, Q., & Lin, P. (2020). A Cartesian cut-cell based multiphase flow model for large-eddy simulation of three-dimensional wave-structure interaction. *Computers & Fluids*, 213, Article 104747. <https://doi.org/10.1016/j.compfluid.2020.104747>
- Yokoi, K., Onishi, R., Deng, X., & Sussman, M. (2016). Density-scaled balanced continuum surface force model with a level set based curvature interpolation technique. *International Journal of Computational Methods*, 13(4), Article 1641004. <https://doi.org/10.1142/S0219876216410048>